

Computational homogenization for multiscale crack modelling. Implementational and computational aspects.

Vinh Phu Nguyen^{1*}, Oriol Lloberas-Valls¹, Martijn Stroeven¹, Lambertus
Johannes Sluys¹

¹*Delft University of Technology, Faculty of Civil Engineering and Geosciences, P.O. Box 5048, 2600 GA
Delft, The Netherlands*

SUMMARY

A computational homogenization procedure for cohesive and adhesive crack modelling of materials with a heterogeneous microstructure has been recently presented in *Comput. Methods Appl. Mech. Engrg.* 2010; DOI:10.1016/j.cma.2010.10.013. The macroscopic material properties of the cohesive cracks are obtained from the inelastic deformation manifested in a localization band (modelled with a continuum damage theory) at the microscopic scale. The macroscopic behavior of the adhesive crack is derived from the response of a microscale sample representing the microstructure inside the adhesive crack. In this manuscript, we extend the theory presented in *Comput. Methods Appl. Mech. Engrg.* 2010; DOI:10.1016/j.cma.2010.10.013 with implementation details, solutions for cyclic loading, crack propagation, numerical analysis of the convergence characteristics of the multiscale method and treatment of macroscopic snapback in a multiscale simulation. Numerical examples including crack growth simulations with extended finite elements are given to demonstrate the performance of the method. Copyright © 2000 John Wiley & Sons, Ltd.

KEY WORDS: representative volume element (RVE), quasi-brittle materials, softening, multiscale, computational homogenization, cohesive law, fracture, XFEM, interface elements

1. INTRODUCTION

Homogenization of heterogeneous materials has been the subject of intensive research over the past decades. A particular homogenization method, computational homogenization (CH) [1], has been utilized to predict mechanical behavior of materials having complex microstructures, see [2, 3, 4, 5] among others. Not only mechanical problems describing linear and nonlinear deformations but also thermal problems [6, 7] and multi-physics (thermo-mechanical) problems [8] have recently been addressed by this method. Other applications encompass thin structures [9, 10, 11, 12, 13]. A unified variational basis of CH theory for bulk materials has been recently presented in [14]. When implemented in a finite element (FE) framework, the method is known as an FE² [15] scheme or, more generally, a multilevel finite element method [16].

*Correspondence to: v.p.nguyen@tudelf.nl Delft University of Technology, Faculty of Civil Engineering and Geosciences, P.O. Box 5048, 2600 GA Delft, The Netherlands

Before [17], studies on homogenization have focussed mainly on determining the effective properties of the macroscopic bulk materials. In [17], the authors developed a computational homogenization scheme for a material layer possessing a heterogeneous microstructure. The behavior of the macroscale material layer (the macro-layer follows an initially elastic cohesive law) is coming from microscale FE computations in which the microstructure is explicitly discretized. Following studies include [18, 19, 20, 21]. According to [22], a review of recent developments of CH methods, homogenization for material layers is qualified as homogenization towards (initially elastic) cohesive laws.

Although computational homogenization has been used with great success in predicting behaviour of many nonlinear heterogeneous materials, when it is used for softening materials the method seems to be of limited use. One major reason is that the homogenized response is not objective with respect to the size of the micro-sample (known as representative volume element (RVE)) used to define the microscale boundary value problem (BVP)- the larger the micro-samples the more brittle the macroscopic response is. **In other words, the RVE does not exist when using standard computational homogenization techniques on softening materials, as stated in [23].** The second reason, not less important, is the sensitivity of the macroscale response with respect to the macroscale discretization due to softening (the macroscopic BVP is ill-posed) [24]. In [24] this problem is solved by a coupled-volume technique in which regularization is preserved in the micro-sample which is coupled in size to the macroscale element. To overcome this second drawback, in [25, 26] a macroscale localization band of fixed width is inserted upon microscale localization. The latest development of this method can be found in [27]. A somewhat similar method, the multiscale aggregating discontinuity (MAD) method, has been presented in [28, 29] in which a crack is introduced at the macroscale when material stability is lost, the crack direction and its opening are all derived from the microscale information. Those methods work well for materials with a periodic microstructure (because the RVE is well defined as a unit cell), **particularly** for masonry in [25, 26] and for fiber reinforced composite in [28, 29]. If the methods are about to be utilized for materials with a random microstructure, sensitivity of the method with respect to the size of the micro-sample should be checked. Recently, a multiscale method for impact modelling of viscoelastic solids having a random microstructure that contains a field of evolving microcracks has been given in [30].

In [31], a new CH scheme for crack modelling which is objective with respect to the micro-sample size has been presented. The method does not suffer from the two aforementioned drawbacks of standard CH methods. It is however restricted to discrete cracking at the microscale. This means that the behavior of a macroscopic cohesive crack is derived from an opening micro-crack. In [32], the authors presented a similar method which is suitable for many quasi-brittle softening materials such as soil and concrete which show damage to be smeared over a zone at the microscale. In this method, the behavior of a macroscopic cohesive crack is coming from the inelastic deformation of a microscale localization band (modelled, for instance, with a continuum damage theory). The method is implemented in a FE² setting in the sense that the constitutive behavior of a material point on the macro-crack is defined during the computation (e.g., *on the fly*) from a microscopic sample. The objectivity of this method with respect to the micro-sample size has been demonstrated in [32] and the existence of an RVE for softening materials has been positively confirmed in [33]. The present manuscript is a continuation of [32].

The new contribution of this paper is three-fold. We first present some implementation

details including a new way to compute the macroscopic tangent. We then discuss the extension of the method to the loading/unloading case and present a simple way to handle macroscopic snapback in a multiscale computation. Finally some numerical examples including crack propagation simulations and convergence characteristics study of the proposed multiscale scheme are given to assess the performance of the method. Possibilities to enhance the computational speed are also discussed.

Methods implemented in the FE² setting are usually classified as multiscale methods with weak coupling between macro- and micro-models. Multiscale modelling of failure of materials with strong coupling between macro- and micro-models has been reported in [34, 35, 36, 37]. For a detailed classification of existing multiscale methods, the reader is referred to [29]. Another multiscale method with strong macro-micro coupling has been given in [38] for elasto-plastic multiphase materials and in [24] for quasi-brittle softening materials. These methods are adequate for moderate jumps between the scales and when the principle of separation of scales between the macroscopic and microscopic length scales does not hold.

The remainder of the paper is structured as follows. In the next section, the finite element models utilized at the macroscale and microscale are discussed together with constitutive laws. Section 3 presents the computational homogenization schemes for adhesive and cohesive cracks. Section 4 describes some implementational and computational aspects of the proposed multiscale crack modelling framework. In the final section, numerical examples are given to demonstrate the performance of the method.

2. MACROSCALE AND MICROSCALE MODELS

In this manuscript, two notations are adopted namely tensor notation and matrix/engineering notation. In matrix notation, the same symbols as for tensors are used to denote the matrices but the connective symbols (used to express the operators) are skipped e.g., the stress-strain relation is written as $\boldsymbol{\sigma} = \mathbf{D} : \boldsymbol{\epsilon}$ in tensor notation and is equivalently (using Voigt notation) written as $\boldsymbol{\sigma} = \mathbf{D}\boldsymbol{\epsilon}$ in matrix notation. **Both macroscale and microscale FE formulations adopt the small-strain kinematics assumption.**

2.1. Macroscale model

Let us consider a two dimensional solid Ω_M shown in Fig.(1) with its boundary denoted by Γ_M . **Prescribed tractions $\bar{\mathbf{t}}$ are imposed on the Neumann boundary $\Gamma_M^t \subseteq \Gamma_M$ whereas prescribed displacements are imposed on the Dirichlet boundary $\Gamma_M^u \subseteq \Gamma_M$.** The discontinuity surface Γ_M^d is composed of cohesive cracks Γ_{coh} and adhesive cracks $\Gamma_{\text{adh}}^\dagger$. It is emphasized that although the material is heterogeneous, the macroscale solid is modelled as **being** homogeneous with effective properties coming from a heterogeneous microscale model.

The discrete equation for quasi-static equilibrium reads

$$\mathbf{f}_M^{\text{ext}} = \mathbf{f}_M^{\text{int}} \equiv \mathbf{f}_M^{\text{bulk}} + \mathbf{f}_M^{\text{coh}} \quad (1)$$

[†]In literature, adhesive cracks are also referred to as adhesive layers, thin material layers or predefined interfaces.

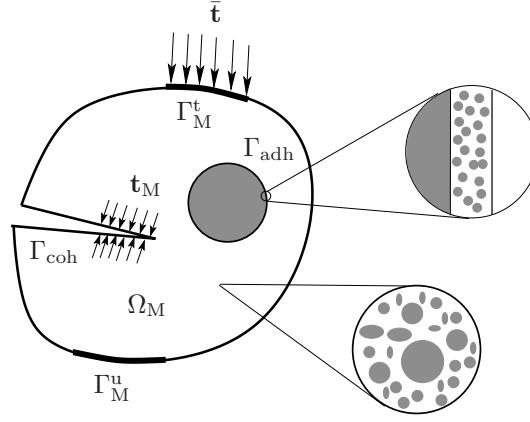


Figure 1. A two dimensional heterogeneous solid containing a cohesive crack and a heterogeneous adhesive crack. **Note that Γ_{coh} represents only the portion of the cohesive crack where \mathbf{t}_M is non-zero.**

where $\mathbf{f}_M^{\text{ext}}$ is the external force vector, $\mathbf{f}_M^{\text{int}}$ is the internal force vector that consists of the bulk force vector $\mathbf{f}_M^{\text{bulk}}$ and the cohesive force vector $\mathbf{f}_M^{\text{coh}}$. They are given by

$$\mathbf{f}_M^{\text{ext}} = \int_{\Omega_M} \mathbf{N}^T \mathbf{b} d\Omega + \int_{\Gamma_M^t} \mathbf{N}^T \bar{\mathbf{t}} d\Gamma \quad (2)$$

$$\mathbf{f}_M^{\text{bulk}} = \int_{\Omega_M} \mathbf{B}^T \boldsymbol{\sigma}_M d\Omega \quad (3)$$

$$\mathbf{f}_M^{\text{coh}} = \int_{\Gamma_M^d} \mathbf{N}^T \mathbf{t}_M d\Gamma \quad (4)$$

where $\boldsymbol{\sigma}_M$ is the macroscale Cauchy stress tensor, \mathbf{b} is the body force vector and \mathbf{t}_M is the cohesive traction across the crack Γ_M^d . In this manuscript, subscripts \square_M and \square_m are used to indicate if a quantity belongs to the macroscale or microscale, respectively. Some macroscale quantities like \mathbf{b} which do not appear at the microscale are written without the subscript M. The strain-displacement matrix \mathbf{B} and the shape function matrix \mathbf{N} , which depend on a specific finite element, are specified without subscript.

For cohesive cracks, a special version of the extended finite element method (XFEM) [39, 40], the phantom node method [41, 42, 43] has been used. Only Heaviside enrichment is used, the cracks thus grow element-wise. For adhesive cracks, we stick to the simpler option of using zero-thickness interface elements (also known as cohesive zone elements or simply cohesive elements) of which details can be found in [44, 45, 46, 47].

2.1.1. Constitutive model The bulk in the vicinity of a cohesive crack is assumed to be linear elastic with effective properties determined in a pre-processing step (before the multiscale simulation starts). That is

$$\boldsymbol{\sigma}_M = \mathbf{D}_0 : \boldsymbol{\epsilon}_M \quad (5)$$

where $\boldsymbol{\epsilon}_M$ is the macroscale strain tensor and \mathbf{D}_0 is the fourth order tensor containing the

effective elastic moduli, which is computed by conventional homogenization theory, we refer to Section 3.1.2 for the procedure.

The behavior of the adherents joined by the adhesive crack is independent of the microstructure of the adhesive crack. It can be modelled with any constitutive laws. However for the sake of this paper, the adherents are assumed to be linear elastic.

The behavior of the macroscale cohesive and adhesive cracks is coming from the microscale models. Thus the macroscale cohesive law is generally given by

$$\mathbf{t}_M = \Phi([\mathbf{u}]_M, \boldsymbol{\sigma}_m) \quad (6)$$

where $[\mathbf{u}]_M$ is the displacement jump across the macro-crack and $\boldsymbol{\sigma}_m$ is the microscale stress tensor. Note that for a cohesive crack, the cohesive law $(\mathbf{t}_M, [\mathbf{u}]_M)$ is initially rigid while for an adhesive crack, $(\mathbf{t}_M, [\mathbf{u}]_M)$ is initially elastic. These are referred to as extrinsic and intrinsic cohesive models according to [48].

2.1.2. Macroscale cohesive tangent The equilibrium equation (1) is solved in an incrementally iterative manner for the macroscale **nodal displacements** \mathbf{u}_M . At Newton-Raphson iteration i for a given load step, one has to solve the linear system $\mathbf{K}_M^{i-1} \Delta \mathbf{u}_M^i = \mathbf{f}_M^{\text{int}, i-1} - \mathbf{f}_M^{\text{ext}}$. Contributions to the macroscale tangent stiffness matrix \mathbf{K}_M include the bulk stiffness and cohesive stiffness matrices. The formula of the former is standard and hence not reported here. The latter is given by

$$\mathbf{K}_M^{\text{coh}} = \int_{\Gamma_M^d} \mathbf{N}^T \mathbf{T}_M \mathbf{N} d\Gamma \quad (7)$$

with \mathbf{T}_M , the macroscale cohesive tangent, defined as

$$\mathbf{T}_M = \frac{\partial \Phi}{\partial [\mathbf{u}]_M} \quad (8)$$

2.2. Microscale model

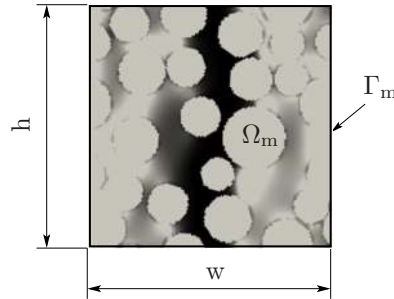


Figure 2. Microscale model: random heterogeneous material undergoing localized damage. The contour plot shows the damage field (white color for undamaged material and black color for completely damaged material).

The microscale model, shown in Fig.(2), is a $w \times h$ rectangular domain Ω_m with external boundary Γ_m where the heterogeneities are explicitly resolved. Geometry of the micro-model (w, h and morphology of the microstructural constituents) depends on whether the macroscale crack to which this micro-model is associated is cohesive or adhesive, see Fig.(1). Let us denote the characteristic length of the micro-constituents as d (e.g., the mean diameter of the inclusions in a matrix/inclusion material) then the dimension of the microscale model must be large enough i.e., $w, h \gg d$ in order for the homogenized quantities to become independent of the microstructural randomness. When this condition is fulfilled, our proposed CH scheme is objective with respect to the micro-sample size.

2.2.1. Constitutive model Damage of the microstructural constituents is modelled by a simple isotropic damage model. The stress-strain relation is given by [49]

$$\boldsymbol{\sigma}_m = (1 - \omega) \mathbf{D}_m^e : \boldsymbol{\epsilon}_m \quad (9)$$

where ω is the scalar damage variable ($0 \leq \omega \leq 1$) and the fourth order tensor \mathbf{D}_m^e contains the elastic moduli. The microscale strain tensor is denoted by $\boldsymbol{\epsilon}_m$. Damage is governed by the following exponential law [50]

$$\omega = 1 - \frac{\kappa}{\kappa_I} [1 - \alpha + \alpha \exp^{-\beta(\kappa - \kappa_I)}], \quad \kappa \geq \kappa_I \quad (10)$$

where α (residual stress), β (softening slope) and κ_I (damage threshold) denote the inelastic parameters. **In the above, the history variable κ evolves according to the Kuhn-Tucker conditions**

$$f \leq 0, \quad \dot{\kappa} \geq 0, \quad \dot{\kappa} f = 0 \quad (11)$$

for the loading function $f = \bar{\epsilon}_{\text{eq}} - \kappa$ where $\bar{\epsilon}_{\text{eq}}$ is the so-called non-local equivalent strain. This loading function is evaluated at integration points.

2.2.2. FE model at the microscale To regularize the local damage model given above, we utilize the implicit gradient enhanced formulation presented in [51] in which the non-local equivalent strain $\bar{\epsilon}_{\text{eq}}$ is computed from the local equivalent strain ϵ_{eq} according to

$$\bar{\epsilon}_{\text{eq}} - c \nabla^2 \bar{\epsilon}_{\text{eq}} = \epsilon_{\text{eq}} \quad (12)$$

For tensile failure studied in this work, ϵ_{eq} follows the Mazars definition [50] and c is a positive valued parameter of the dimension length squared. Equation (12) is solved with the boundary condition $\nabla \bar{\epsilon}_{\text{eq}} \cdot \mathbf{n} = 0$ on Γ_m where \mathbf{n} is the outward unit normal at the boundary Γ_m . A discussion on potential consequences of this boundary condition to the non-local interactions between microstructural phases is given in [33]. Note that the multiscale framework presented in this work is not restricted to the gradient enhanced regularization type given in Eq.(12). Other regularization methods such as the integral type non-local theory [52] or the viscous regularization approach [53] can be equally utilized as well.

The FE equations read [51]

$$\int_{\Omega_m} \mathbf{B}_u^T \boldsymbol{\sigma}_m d\Omega = \mathbf{f}_m^{\text{ext}}(\llbracket \mathbf{u} \rrbracket_M) \quad (13a)$$

$$\int_{\Omega_m} \mathbf{N}_\epsilon^T \mathbf{N}_\epsilon \bar{\boldsymbol{\epsilon}}_{\text{eq}} d\Omega + \int_{\Omega_m} \mathbf{B}_\epsilon^T c \mathbf{B}_\epsilon \bar{\boldsymbol{\epsilon}}_{\text{eq}} d\Omega = \int_{\Omega_m} \mathbf{N}_\epsilon^T \epsilon_{\text{eq}} d\Omega \quad (13b)$$

where \mathbf{B}_u is the standard strain-displacement matrix, \mathbf{N}_ϵ is a row vector containing the shape functions used to discretize $\bar{\boldsymbol{\epsilon}}_{\text{eq}}$ and $\mathbf{B}_\epsilon = \nabla \mathbf{N}_\epsilon$. **It is emphasized that the RHS of Eq.(13a) is different from the formulation given in [51]. In the proposed multiscale scheme, since the micro model is coupled to an integration point on the macro-crack, it is loaded by the displacement jump of this integration point. Thus, the microscopic external force vector depends on the macroscopic displacement jump.** Note that at the microscale, the inertia force and the body force can be neglected as suggested in [54].

Equation (13) can be written in a general format as

$$\mathbf{f}_m^{\text{int}}(\mathbf{u}_m) = \mathbf{f}_m^{\text{ext}}(\llbracket \mathbf{u} \rrbracket_M) \quad (14)$$

with \mathbf{u}_m is the microscale nodal unknowns vector. Note that \mathbf{u}_m contains both nodal displacements and nodal non-local equivalent strain degrees of freedom (dofs) $\bar{\boldsymbol{\epsilon}}_{\text{eq}}$. **Note that the bold symbol $\bar{\boldsymbol{\epsilon}}_{\text{eq}}$ indicates the nodal values of the corresponding non-local equivalent strain field $\bar{\boldsymbol{\epsilon}}_{\text{eq}}$.**

3. MACRO-MICRO COUPLING

3.1. Macro-micro coupling for cohesive cracks

The problem that we are solving is that given a displacement jump $\llbracket \mathbf{u} \rrbracket_M$ of an integration point on the macro-crack, find the corresponding traction \mathbf{t}_M . Borrowing ideas from conventional CH theory for the bulk of the solid, this is achieved by transforming $\llbracket \mathbf{u} \rrbracket_M$ to a microscale model which is associated to this integration point[‡], the microscale BVP is then solved. The macro-traction \mathbf{t}_M is defined as a function of the microscale stresses. Figure (3) shows the multiscale cohesive crack modelling framework using computational homogenization.

The difficulty lies in how to define such a link which yields an objective macroscopic response with respect to the size of the micro-sample in the sense that when the micro-sample is large enough to be independent of the microstructural randomness, larger samples will lead to the same response. It has been shown in [33, 32] that by extracting the microscale response in the loading damaged domain (rather than in the entire microscale domain as done in conventional homogenization theory), the homogenized response becomes independent of the micro-model size as long as the micro-sample is sufficiently large so that the homogenized properties are independent of the microstructural randomness. This is achieved by the recently emerged failure zone averaging technique [33] which is briefly described in what follows.

[‡]To reduce the implementation complexity and computer resources, in this work, it has been assumed that the RVEs for all integration points on a macro-crack are identical.

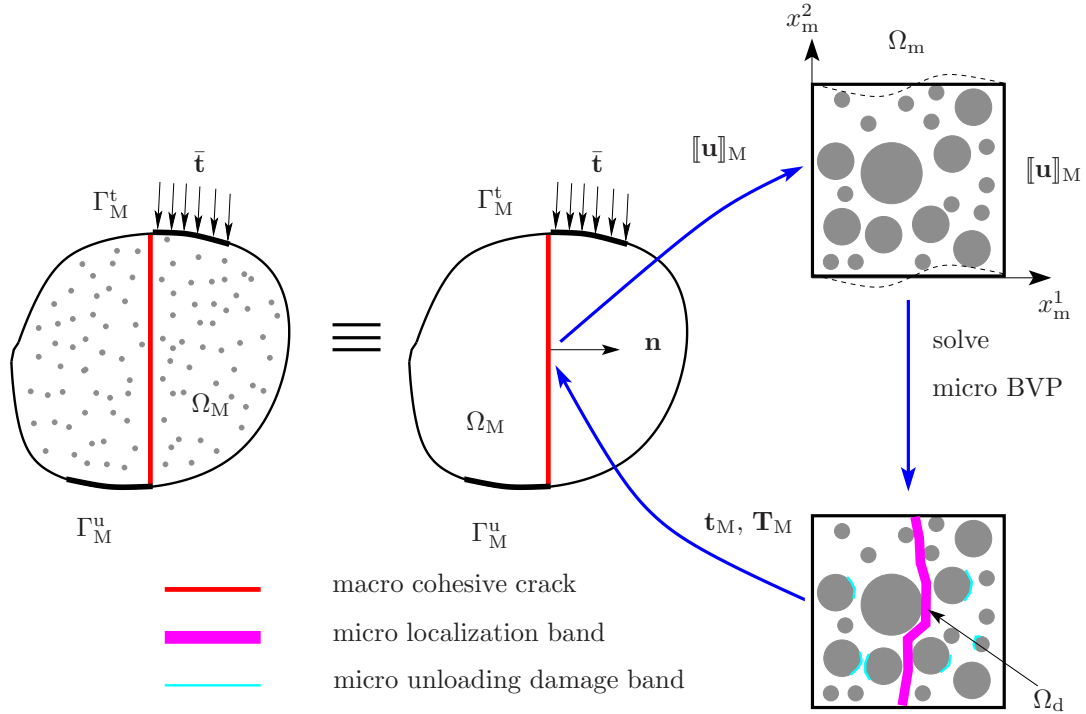


Figure 3. Schematic representation of the multiscale cohesive crack scheme.

Let us first denote Ω_d as the microscale region containing Gauss points which are damaged and loading. Mathematically Ω_d is defined as

$$\Omega_d = \{\mathbf{x} \in \Omega_m \mid \omega(\mathbf{x}) > 0, f(\mathbf{x}) = 0\} \quad (15)$$

where f is the loading function, see Section 2.2.1. **The active damaged domain is computed as the accumulated tributed area of all Gauss points that are damaged and loading.**

The homogenized strain $\langle \epsilon \rangle_{\text{dam}}$ is then defined as the volume average of its microscale counterpart over Ω_d

$$\langle \epsilon \rangle_{\text{dam}} = \frac{1}{|\Omega_d|} \int_{\Omega_d} \epsilon_m d\Omega \quad (16)$$

where $|\cdot|$ denotes the measure of the domain. This domain integral is computed using the same numerical quadrature rule that is used to integrate the microscale stiffness matrices.

We define the displacement of this active damaged domain Ω_d as the projection of $\langle \epsilon \rangle_{\text{dam}}$ on the macro-crack plane

$$\mathbf{u}_{\text{dam}} = \langle \epsilon \rangle_{\text{dam}} \cdot (l\mathbf{n}), \quad l = \frac{|\Omega_d|}{h} \quad (17)$$

where l is the averaged width of the localization band Ω_d and \mathbf{n} is the outward unit normal vector of the crack. **Note that this expression was obtained for the case in which the localization**

band cuts the micro sample at two points, one on the lower edge and the other on the upper edge, see Fig. (3). This is, however, a valid assumption considering mode I failure studied in this work.

It has been shown in [32] that the $(\mathbf{t}_M, \mathbf{u}_{\text{dam}})$ curves are objective with respect to the size of the micro-model exhibiting one dominant localization band. This is the case for materials having a random complex microstructure in tensile and shear loadings. Therefore, if $[\mathbf{u}]_M$ is defined to be equal to \mathbf{u}_{dam} , we obtain an objective macroscale cohesive law $(\mathbf{t}_M, [\mathbf{u}]_M)$. The final homogenization relation is given by

$$\mathbf{u}_R = [w - l]\mathbf{C}_0 \cdot \mathbf{t}_M + [\mathbf{u}]_M + \dot{\mathbf{u}}_{\text{dam}} \quad (18)$$

where \mathbf{C}_0 is the projection of the compliance tensor \mathbf{D}_0^{-1} on the macro-crack plane and \mathbf{u}_R is the displacement of the right edge of the RVE. In the above, $\dot{\mathbf{u}}_{\text{dam}}$ is \mathbf{u}_{dam} evaluated at the moment that microscale softening occurs which is defined as the moment that first negative eigenvalues of \mathbf{T}_M are detected, see [32] for the derivation details. Note that the first term on the RHS of the above equation is the linear part of the total microscale displacement. **It should be mentioned that Eq. (18) resembles Equation (19) in [31] in the limiting case of l going to zero (which is indeed the case in [31] as discrete micro cracking is assumed).**

For macroscale load step n and macroscale Newton-Raphson iteration i , at a Gauss point gp with $[\mathbf{u}]_M$, the system of equations at the microscale is thus given by

$$\begin{aligned} \mathbf{f}_m^{\text{int}}(\mathbf{u}_m) &= \mathbf{f}_m^{\text{ext}}([\mathbf{u}]_M) \\ \mathbf{u}_R(\mathbf{u}_m) &= [w - l]\mathbf{C}_0 \cdot \mathbf{t}_M + [\mathbf{u}]_M + \dot{\mathbf{u}}_{\text{dam}} \end{aligned} \quad (19)$$

which is solved for the microscale nodal unknowns \mathbf{u}_m and the macro-traction \mathbf{t}_M . This system of equations is solved iteratively by first imposing an initial displacement on the micro-model, then the microscale equilibrium equation Eq.(19)₁ is solved, next Eq.(19)₂ is checked. If it is not satisfied, a new value of the initial displacement is calculated and the process is repeated until both equations of Eq.(19) are satisfied. More details on the process can be found in [32]. Box (1) shows the pseudocode of the multiscale crack framework. Note that during step (A) in Box (1) the microscale BVP must be solved $p > 1$ times. This is a crucial difference between the proposed method and the standard FE² method.

The macro-traction \mathbf{t}_M and macroscale cohesive tangent matrix \mathbf{T}_M are derived in [32] and are given by, respectively

$$\mathbf{t}_M = \frac{1}{h} \sum_{I=1}^{n_b} \mathbf{f}_{m,I}^{\text{int}} \quad (20a)$$

$$\mathbf{T}_M = \frac{1}{h} \mathbf{M}^T \mathbf{K}_m^{*,R} \mathbf{M} \quad (20b)$$

where n_b is the number of nodes on the right edge of the micro-sample where the boundary conditions (BCs) are applied (details on BCs of the micro-model are given in Section 3.3) and the $[2n_b \times 2]$ matrix \mathbf{M} is given by

$$\mathbf{M} = \begin{bmatrix} 1 & 0 & 1 & 0 & \cdots & 1 & 0 \\ 0 & 1 & 0 & 1 & \cdots & 0 & 1 \end{bmatrix}^T \quad (21)$$

Box 1 Flowchart of the multiscale crack framework implemented in a FE² setting.

1. For a macroscale load step n and Newton-Raphson iteration i do

- (a) Loop over elements to compute $\mathbf{f}_M^{\text{coh}}$ ⁽¹⁾
- i. Loop over integration points on the crack segment
 - Get the macro-jump $\llbracket \mathbf{u} \rrbracket_M$
 - Compute \mathbf{t}_M and \mathbf{T}_M with microscale computations
 - A. Solve the micro-problem given in Eq.(19) ⁽²⁾
 - B. Compute the macro-traction \mathbf{t}_M via Eq.(20a)
 - C. Compute the macro-tangent \mathbf{T}_M via Eq.(20b)
 - Compute $\mathbf{f}_M^{\text{coh}}$ using \mathbf{t}_M
 - Compute $\mathbf{K}_M^{\text{coh}}$ using \mathbf{T}_M
 - ii. End loop over integration points
- (b) End loop over elements

2. Proceed to the next iteration

3. Upon convergence of load step n , commit the state of all micro-models.

⁽¹⁾ Computation of the bulk contribution $\mathbf{f}_M^{\text{bulk}}$ is done as in standard FEM.

⁽²⁾ With state (nodal unknowns and internal variables) being reset to its previous converged values.

The $[2n_b \times 2n_b]$ matrix $\mathbf{K}_m^{*,R}$ is the microscale stiffness matrix associated to the right edge displacement dofs. Details on how to compute this matrix and thus \mathbf{T}_M are given in Section 4.2. Note that \mathbf{T}_M is generally not symmetric because the microscale stiffness matrix is non-symmetric due to the adopted damage constitutive law.

3.1.1. Crack initiation/propagation criterion Following [31] the initiation/propagation criterion and the growth direction for the macroscale cohesive crack is purely macroscopic i.e., the macro-crack propagates based on the macroscale stress field. However note that microstructural effects have a contribution to the macro-crack initiation/propagation because the macroscale stress field is computed from the effective properties, see Eq.(5). We utilize the maximum principal stress criterion as the crack initiation/propagation indicator and the non-local stresses, **computed as a weighted average of stresses**, at the crack tip to determine the crack direction as proposed in [40]. Note that in [28, 27, 29] the macro-crack direction has been computed using information from the micro-model. In our opinion, this only makes sense when the microscopic length scale is of the same magnitude as the macroscopic length scale.

Remark 3.1. *The works in [25, 26] have used a failure criterion based on microscopic information for the macroscopic crack initiation/propagation. In our scheme, since only the macroscopic crack and not the macroscopic bulk is coupled to an RVE, we could not use such a microscopic failure criterion. For quasi-brittle heterogeneous materials, the utilization of the elastic macroscopic stresses as the driving force for crack initiation suffers from two disadvantages (i) the pre-failure hardening stage cannot be captured and (ii) the predicted peak is overshoot. Extension of the current multiscale scheme is reported in [55] in which*

macro-crack initiation is based on a microscopic localization criterion. We refer to Remark 3.3 for a discussion on when the macroscopic stresses can be reasonably adopted to drive crack initiation/propagation.

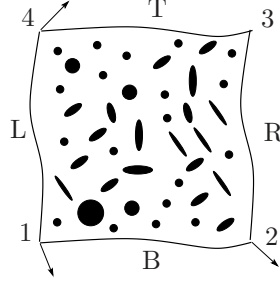


Figure 4. Boundary conditions imposed on a micro model to compute the effective elasticity constants.

3.1.2. Effective elasticity constants The effective elastic moduli tensor \mathbf{D}_0 can be determined using either analytical or computational homogenization theory. While the former is applicable to micro-samples with simple morphology such as circular or elliptical inclusions, the latter can be used for any kind of microstructure and therefore is chosen in this work. Details can be found in [5], here for sake of completeness, key equations are given. The BCs of the micro-model consist of periodic boundary conditions Eq.(22), see Fig.(4), and prescribed displacements Eq.(23)

$$\begin{aligned} \mathbf{u}_T &= \mathbf{u}_B + \mathbf{u}_4 - \mathbf{u}_1 \\ \mathbf{u}_R &= \mathbf{u}_L + \mathbf{u}_2 - \mathbf{u}_1 \end{aligned} \quad (22)$$

with prescribed displacements for the corner nodes $q = 1, 2, 4$ defined as

$$\mathbf{u}_q = \boldsymbol{\epsilon}_M \cdot \mathbf{x}_{q,m} = \mathbf{D}_q^T \boldsymbol{\epsilon}_M, \quad \mathbf{D}_q = \frac{1}{2} \begin{bmatrix} 2x_m^1 & 0 \\ 0 & 2x_m^2 \\ x_m^2 & x_m^1 \end{bmatrix}_q \quad (23)$$

where we have switched to matrix-vector notation in the second equality. In the above, $\mathbf{x}_{q,m}$ denotes the nodal coordinates of node q with respect to the microscopic coordinate system $x_m^1 - x_m^2$, cf. Fig. (3).

The effective elastic tangent moduli \mathbf{D}_0 is given by

$$\mathbf{D}_0 = \frac{1}{|\Omega_m|} \mathbf{D} \bar{\mathbf{K}}_{qq} \mathbf{D}^T, \quad \mathbf{D} = [\mathbf{D}_1 \ \mathbf{D}_2 \ \mathbf{D}_4] \quad (24)$$

where the 6×6 matrix $\bar{\mathbf{K}}_{qq}$ is obtained via a condensation of the microscale stiffness matrix. Details can be found in [5].

In summary, to compute \mathbf{D}_0 , we impose a strain vector $[\bar{\epsilon}, 0, 0]$ to three corner nodes 1, 2 and 4 of the micro-mesh. The microscale BVP (for the effective elastic properties, the microscale BVP is simply a linear elasticity problem) is then solved with periodic BCs. The converged linear

system of equations is condensed out to obtain $\bar{\mathbf{K}}_{qq}$ and equation (24) is used to compute \mathbf{D}_0 . Note that \mathbf{D}_0 is symmetric due to the fact that the microscopic stiffness matrix is symmetric.

Remark 3.2. *It is worth noting that, for materials with a random heterogeneous microstructure, the dimension of the micro-model used to compute the elastic effective properties may differ from the dimension of the micro-model used to determine the macroscale cohesive law.*

3.1.3. Tensile strength of the homogenized material Evaluation of the maximum stress criterion requires the tensile strength of the homogenized material. In the homogenization multiscale scheme, this value is defined as the ultimate load of the micro-model σ_m^{ult} subjected to a horizontal tensile loading. In other words, in a pre-processing step, one micro-model is loaded in tension along the horizontal direction (BCs are described in Section 3.3) and its ultimate load is computed as

$$\sigma_m^{\text{ult}} = \frac{1}{h} \sum_{I=1}^{n_b} \mathbf{f}_{m,I}^{\text{int}}(\tau) \quad (25)$$

τ denotes the instance at which the peak is attained.

3.1.4. Micro model activation Unlike the conventional homogenization approach for the bulk material and for an adhesive crack in which a micro-model is linked to a macroscale integration point *ab initio*, in the multiscale cohesive crack scheme presented in this work, a micro-model is brought into the scene when a new crack segment is initiated. Since the behavior of that new crack segment comes only from the softening regime of the micro-model, this micro-model must be loaded from an undeformed state to its peak. To this end, the micro-model is loaded, under load control, from zero up to $\bar{f} = \gamma \sigma_m^{\text{ult}} h^{\S}$ together with homogeneous BCs and periodic BCs as described in Section 3.3 with $\gamma = 1 - \epsilon$, where ϵ is a small positive number, is introduced to ensure convergence of this activation step. Furthermore, nodes on the right edge of the micro-model are forced to undergo the same displacement as shown in Fig.(5). After being activated, the micro-model is loaded in displacement control, thus the force \bar{f} and the aforementioned constraint are removed. This implies that the crack initiation/propagation criterion now reads $\sigma_M^I \geq \gamma \sigma_m^{\text{ult}}$ where σ_M^I denotes the maximum macroscale principal stress.

The coupling between the macro-model and the micro-model is summarized in Fig.(6). Note that the pre-failure nonlinear (hardening) part of the micro-model, indicated in Fig.(6) by the darker region, is not captured by the macro-model. Therefore, an assumption was made that this hardening part is negligible. As can also be seen, the homogenized cohesive law is not strictly initially rigid but has a small hardening portion.

Remark 3.3. *When the assumption on the negligibility of the microscopic hardening part does not hold, modifications to the proposed scheme should be made. One option is to compute the macroscale bulk constitutive model on the fly as well. After crack nucleation, the macroscale bulk integration points are no longer coupled to the micro-models but follow a linear elastic*

^{\S}This is achieved by dividing \bar{f} into a number of sub-steps to ensure convergence.

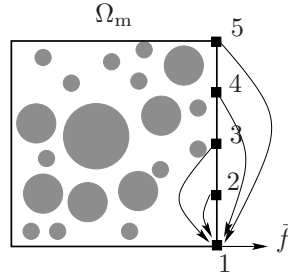


Figure 5. Force control to activate the micro-model upon cohesive crack insertion. A force is applied on node 1 whereas other nodes on the right edge are forced to have the same displacement as node 1.

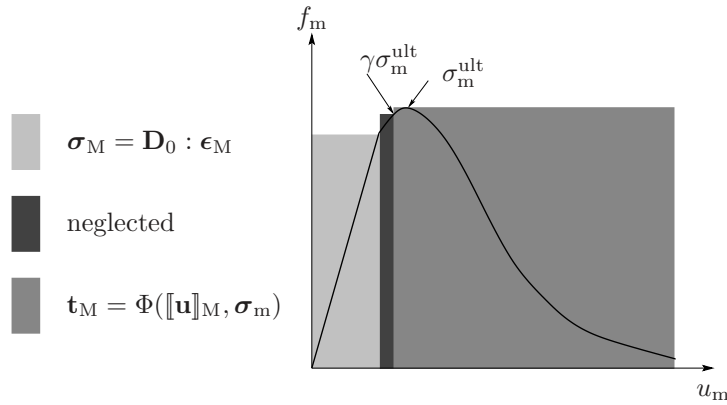


Figure 6. Coupling between macro- and micro-models for cohesive crack modelling.

law with effective properties evaluated at the crack nucleation moment. This option shares similarity with the method given in [27]. However this is beyond the scope of this manuscript and is presented in [55].

3.1.5. Principle of scale separation This section discusses the issue of the principle of scale separation in the cohesive crack multiscale model. Let us recall that there are two quantities that are averaged in the proposed model- the bulk material surrounding the crack and the crack itself. The principle of scale separation applies for the bulk homogenization requires that the dimension of the micro-sample (for bulk homogenization) must be much smaller than the macroscopic lengthscale so that the macroscale fields (stress or strain) are uniform over the micro-sample. For the crack homogenization, in order to satisfy the principle of scale separation, the micro-sample should be small enough compared to the macroscale fracture process zone (FPZ) so that the averaged quantities (e.g., \mathbf{t}_M or $[[\mathbf{u}]]_M$) are constant over it. Since the FPZ is not known *a priori*, this condition is currently checked only *a posteriori*. One potential solution is that for cohesive integration points in the FPZ, if the principle of scale separation does not hold, micro-models with smaller dimension are used. This kind of RVE-size adaptivity is a topic of future research.

3.2. Macro-micro coupling for adhesive cracks

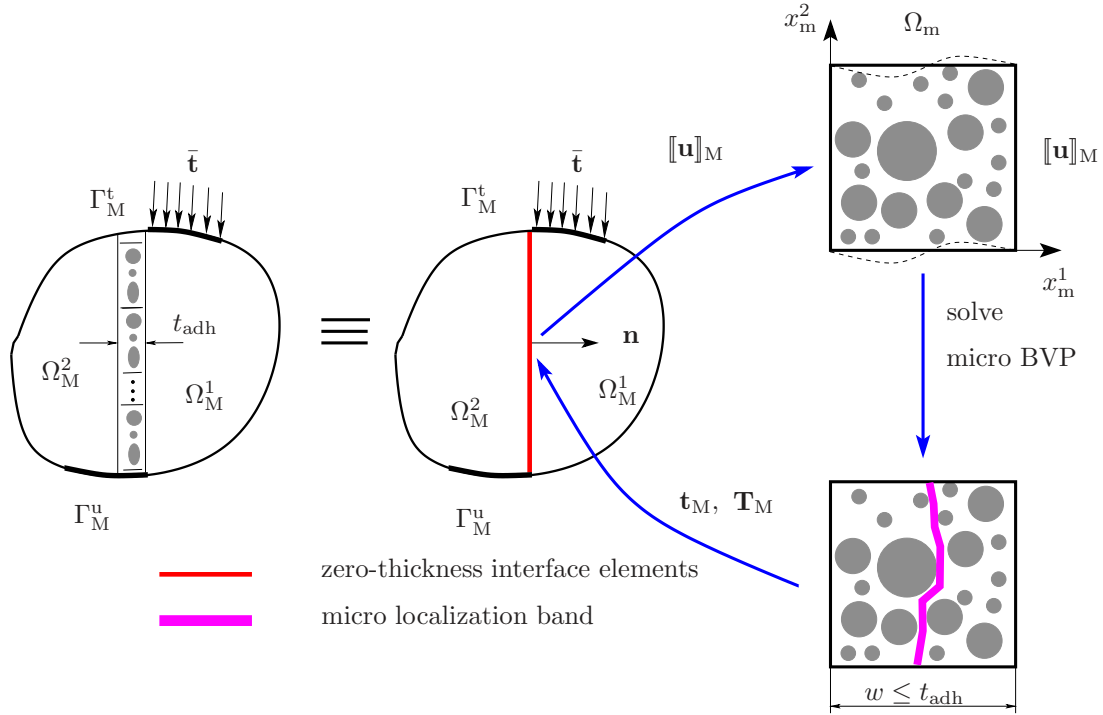


Figure 7. Schematic representation of the multiscale adhesive crack scheme.

Figure (7) presents the scheme of the multiscale framework for an adhesive crack of thickness t_{adh} that joints two adherents Ω_M^1 and Ω_M^2 . The behavior of the adhesive crack is determined by means of a micro-model that represents the microstructure inside the crack. The case in which the micro-model width w is equal to t_{adh} is referred to as case I whereas the case in which $w < t_{adh}$ is denoted as case II, following the convention adopted in [31].

3.2.1. Case I When the micro-model width w equals t_{adh} , one has $\mathbf{u}_R = \llbracket \mathbf{u} \rrbracket_M$. The multiscale scheme is thus trivial. The macro-jump is directly imposed on the right edge of the RVE, the microscale BVP is solved. The macro-traction and the macroscale cohesive tangent are computed via Eqs.(20a) and (20b). This scheme was first presented in [17] for small strain problems and later in [18] for finite deformations and shares similarity with the one given in [21].

3.2.2. Case II The homogenization relation for an adhesive crack in case that the micro-model width is smaller than the adhesive crack thickness i.e., $w < t_{adh}$ has been first derived in [31] for microscale discrete cracking and then in [32] for microscale localized damage. The final equation is the same and is given by

$$\mathbf{u}_R = (w - t_{adh})\mathbf{C}_0 \cdot \mathbf{t}_M + \llbracket \mathbf{u} \rrbracket_M \quad (26)$$

which provides the homogenization relation between microscale information and the macroscale cohesive law $(\mathbf{t}_M, \llbracket \mathbf{u} \rrbracket_M)$. Comparing this expression with Eq.(18) (for cohesive cracks) shows that Eq.(26) can be obtained from Eq.(18) with $l = t_{adh}$ (the compliance is now scaled with t_{adh}) and $\dot{\mathbf{u}}_{dam} = 0$ (since the adhesive crack is present in the macro-model at the onset of the simulation).

The system of equations needs to be solved at the microscale is thus given by

$$\begin{aligned} \mathbf{f}_m^{\text{int}}(\mathbf{u}_m) &= \mathbf{f}_m^{\text{ext}}(\llbracket \mathbf{u} \rrbracket_M) \\ \mathbf{u}_R(\mathbf{u}_m) &= (w - t_{adh})\mathbf{C}_0\mathbf{t}_M + \llbracket \mathbf{u} \rrbracket_M \end{aligned} \quad (27)$$

that consists of the microscale equilibrium Eq.(14) and the homogenization relation Eq.(26). This system of equations is solved using an iterative scheme that is similar to the one for cohesive cracking, the reader is referred to [32] for details. However it is emphasized that the above system of equations is different from the one for the cohesive crack, Eq.(19), in the sense that while the latter filters out the microscopic linear response so that the macro-jump equates the microscale inelastic displacements, the former adjusts the microscopic linear displacements so that the case II solution matches the case I solution.

It is emphasized that since the homogenization relation given in Eq.(26) is only applicable to the softening regime, Eq.(27) only ensures that its solution in the softening regime coincides the solution obtained with the case I algorithm (for the same considered problem). The linear regime is solved using the case I algorithm but with $\mathbf{u}_R = (w/t_{adh})\llbracket \mathbf{u} \rrbracket_M$ [¶]. The transition from the linear regime to the softening regime is detected by the appearance of negative eigenvalues of the macro cohesive tangent \mathbf{T}_M [25].

The flowchart for the multiscale adhesive crack schemes is almost identical to the one for cohesive cracks, cf. Box (1). The only differences lies in step (A)- solving Eq.(14) for the case I scheme and solving Eq.(27) for the case II scheme. A discussion on the trade-offs of using the case I or case II scheme for a given problem has been given in [32].

Remark 3.4. *Although the homogenization equation (26) resembles the equation that was derived in [31], we briefly presented the scheme for adhesive crack multiscale modelling due to the following reasons. The case I scheme is exactly the same and given here merely for completeness. For the case II scheme, [31] considered microscopic discrete cracking while we are studying microscopic diffusive damage. Furthermore, note that our iterative scheme used to solve Eq.(27) is different from the solution technique adopted in [31].*

3.3. Boundary conditions of the microscale model

Boundary conditions of the boundary nodes of a micro-mesh are given by

$$\begin{aligned} \text{periodic BCs} & : \mathbf{u}_T = \mathbf{u}_B + \mathbf{u}_2 - \mathbf{u}_1 \\ \text{fixed BCs} & : \mathbf{u}_L = \mathbf{0} \\ \text{prescribed BCs} & : \mathbf{u}_R = g(\llbracket \mathbf{u} \rrbracket_M) \end{aligned} \quad (28)$$

[¶]This guarantees that the linear responses obtained by case I and case II algorithms are identical, see [32] for explanation.

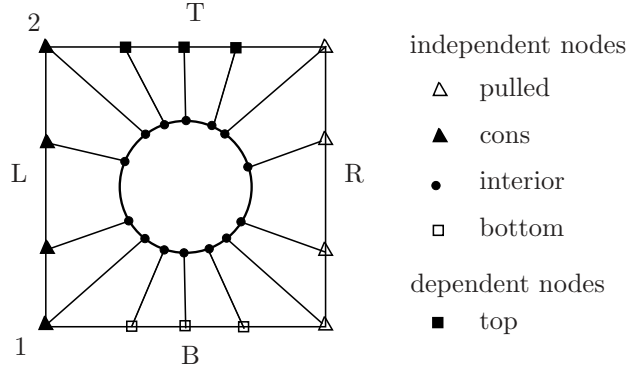


Figure 8. Illustration of various node groups in a simple micro-mesh.

see Fig.(8) for notations. In the above, \mathbf{u} indicates the microscale displacement dofs, $g(\llbracket \mathbf{u} \rrbracket_M) = \llbracket \mathbf{u} \rrbracket_M$ for the case I adhesive crack model. For cohesive scheme and the case II adhesive scheme, the reader is referred to [32] for details. Note that these notations will be used in the sequel. This kind of BCs is first given in [17] and referred to as hybrid BCs/semi-periodic BCs in [18].

4. ALGORITHMIC ASPECTS

In this section, various implementation details are presented. Note that the basic implementation of a multilevel FEM can be found elsewhere for instance in [5]. The efficient solution of the microscale nonlinear problem with periodic BCs is discussed first. The extraction of the macroscale cohesive tangent matrix \mathbf{T}_M from the microscale stiffness using the probing method is then presented. The advantage of this method is that it avoids the inversion of a large, sparse matrix and its explicit partition into sub-matrices. Treatment of arbitrary macro-crack orientation i.e., the crack coordinate system is not aligned with the global coordinate system, is also given. To the best of the authors' knowledge, works on homogenization have focused mainly on monotonic loading. Here we present a discussion on computational homogenization for loading/unloading cases. Finally, resolving the snapback at the macroscopic scale with the dissipation-based arc-length control [56] is presented.

4.1. Solution of micro problem

In what follows, the master-slave method, used to solve the microscopic linear system with periodic constraints, is presented in details. It is emphasized that in [18] the same topic has been given. However, we present a somewhat different implementation and this section will be needed in subsequent presentation. In this section, the subscript m (indicating microscale quantities) is omitted for sake of clarity.

Let us first write the periodic BCs given in Section 3.3 in the following format

$$\delta \mathbf{u}_d = \mathbf{C} \delta \mathbf{u}_i \quad (29)$$

where \mathbf{C} is the dependency matrix; subscripts d and i denote dependent and independent

degrees of freedom, respectively, see Fig.(8).

The full microscale nodal unknowns vector can be written in terms of the independent nodal values as

$$\delta \mathbf{u} = \begin{bmatrix} \delta \mathbf{u}_i \\ \delta \mathbf{u}_d \end{bmatrix} = \begin{bmatrix} \mathbf{I} \\ \mathbf{C} \end{bmatrix} \delta \mathbf{u}_i \equiv \mathbf{T} \delta \mathbf{u}_i \quad (30)$$

with \mathbf{I} being the $[3n_i \times 3n_i]$ unit matrix (n_i is the number of independent nodes) and \mathbf{T} being the so-called transformation matrix which is a rectangular matrix.

The microscale linearized system is rearranged as

$$\begin{bmatrix} \mathbf{K}_{ii} & \mathbf{K}_{id} \\ \mathbf{K}_{di} & \mathbf{K}_{dd} \end{bmatrix} \begin{bmatrix} \delta \mathbf{u}_i \\ \delta \mathbf{u}_d \end{bmatrix} = \begin{bmatrix} \mathbf{r}_i \\ \mathbf{r}_d \end{bmatrix} \quad (31)$$

with \mathbf{r} being the residual vector.

By substituting Eq.(30) into the above and pre-multiplying both sides with \mathbf{T}^T we obtain

$$[\mathbf{I} \quad \mathbf{C}^T] \begin{bmatrix} \mathbf{K}_{ii} & \mathbf{K}_{id} \\ \mathbf{K}_{di} & \mathbf{K}_{dd} \end{bmatrix} \begin{bmatrix} \mathbf{I} \\ \mathbf{C} \end{bmatrix} \delta \mathbf{u}_i = [\mathbf{I} \quad \mathbf{C}^T] \begin{bmatrix} \mathbf{r}_i \\ \mathbf{r}_d \end{bmatrix} \quad (32)$$

which yields the sought-for reduced system

$$\mathbf{K}^* \delta \mathbf{u}_i = \mathbf{r}^* \quad (33)$$

with \mathbf{K}^* , a $[3n_i \times 3n_i]$ matrix and \mathbf{r}^* , a $[3n_i \times 1]$ vector, being given by

$$\begin{aligned} \mathbf{K}^* &= \mathbf{T}^T \mathbf{K} \mathbf{T} \\ \mathbf{r}^* &= \mathbf{T}^T \mathbf{r} \end{aligned} \quad (34)$$

Usually Eq.(33) is solved for the independent displacement increments and then the dependent displacement increments are computed via Eq.(29) (e.g., [5, 18]). Here, we prefer solution methods that do not alter the dimension of the stiffness matrix. This has several advantages. First, there is no need to keep track of which dof corresponds to which unknown in the linear solver. Second, there is no need to store a new, constrained matrix (\mathbf{K}^*) if the linear system is solved with an iterative solver. In this case we just keep the original matrix, and apply the matrix \mathbf{T} in each matrix-vector multiplication. A third advantage is that in parallel computations each processor can setup and apply constraints without having to modify the communication data structures in the linear solver. Precisely, the following system is solved instead of Eq.(33)

$$\underbrace{\begin{bmatrix} \mathbf{T}^T \mathbf{K}_m \mathbf{T} & \mathbf{0} \\ \mathbf{0} & \mathbf{I} \end{bmatrix}}_{\bar{\mathbf{K}}_m} \begin{bmatrix} \delta \mathbf{u}_i \\ \delta \mathbf{u}_d \end{bmatrix} = \begin{bmatrix} \mathbf{r}^* \\ \delta \mathbf{u}_d \end{bmatrix} \quad (35)$$

In words, the matrix \mathbf{K}^* has been augmented with the trivial equation $\mathbf{I} \delta \mathbf{u}_d = \delta \mathbf{u}_d$ so that $\bar{\mathbf{K}}_m$ is of the same dimension as \mathbf{K}_m .

||This unit matrix is for 2D. Note that for the gradient enhanced damage model used at the microscale, there are three dofs per node.

Remark 4.1. *The motivation for premultiplying Eq. (31) with \mathbf{T}^T in order to obtain Eq. (32) is as follows. Matrix \mathbf{T} essentially encodes the relationship between the independent dofs and all dofs, including the dependent dofs. This means that matrix $\mathbf{T}^T \mathbf{K} \mathbf{T}$ can be viewed as the projection of matrix \mathbf{K} on a vector space spanned by the independent dofs. In other words, the full system of equations is projected on the vector space spanned by the independent dofs and is then solved for the resulting, smaller system of equations.*

4.2. Probing method to compute the macroscale cohesive tangent

Equation (35) can be written in the following format at the converged state of the microscale BVP

$$\begin{bmatrix} \bar{\mathbf{K}}_m^{aa} & \bar{\mathbf{K}}_m^{ab} & \mathbf{0} \\ \bar{\mathbf{K}}_m^{ba} & \bar{\mathbf{K}}_m^{bb} & \mathbf{0} \\ \mathbf{0} & \mathbf{0} & \mathbf{I} \end{bmatrix} \begin{bmatrix} \delta \mathbf{u}_m^a \\ \delta \mathbf{u}_m^b \\ \delta \mathbf{u}_d \end{bmatrix} = \begin{bmatrix} \mathbf{0} \\ \delta \mathbf{f}_b \\ \delta \mathbf{u}_d \end{bmatrix} \quad (36)$$

with b denoting dofs associated to nodes on the right edge and a are the dofs of the remaining nodes excluding top nodes, see Fig.(8). The above allows the following condensation

$$\mathbf{K}_m^{*,bb} \delta \mathbf{u}_m^b = \delta \mathbf{f}_b \quad (37)$$

with

$$\mathbf{K}_m^{*,bb} = \bar{\mathbf{K}}_m^{bb} - \bar{\mathbf{K}}_m^{ba} (\bar{\mathbf{K}}_m^{aa})^{-1} \bar{\mathbf{K}}_m^{ab} \quad (38)$$

This $[3n_b \times 3n_b]$ matrix can be filtered to get $\mathbf{K}_m^{*,R}$, a $[2n_b \times 2n_b]$ matrix which involves only displacement dofs of the nodes b , as following

$$\mathbf{K}_m^{*,R} = \mathbf{A}^T \mathbf{K}_m^{*,bb} \mathbf{A} \quad (39)$$

where \mathbf{A} is a $[3n_b \times 2n_b]$ boolean matrix. Note that if the FE formulation adopted at the microscopic scale involves only displacement dofs (e.g., in a non-local integral damage model) the above step is skipped.

Substituting Eq.(38) into Eq.(20b) yields

$$\mathbf{T}_M = \frac{1}{h} \mathbf{M}^T \mathbf{A}^T [\bar{\mathbf{K}}_m^{bb} - \bar{\mathbf{K}}_m^{ba} (\bar{\mathbf{K}}_m^{aa})^{-1} \bar{\mathbf{K}}_m^{ab}] \mathbf{A} \mathbf{M} \quad (40)$$

For materials with complex multi-phase microstructures, the microscale stiffness matrix \mathbf{K}_m could be a very large, sparse matrix of which inversion and partition operations are obviously inefficient. In order to avoid them, we use the so-called probing technique that is a very simple technique to construct a matrix, here \mathbf{T}_M , from a series of matrix-vector products. This matrix is built in a columnwise manner. The first column of \mathbf{T}_M is computed by multiplying the RHS of Eq.(40) with $\mathbf{e}_1 = [1 \ 0]^T$

$$\mathbf{T}_M^1 = \frac{1}{h} \mathbf{M}^T \mathbf{A}^T [\bar{\mathbf{K}}_m^{bb} \mathbf{f} - \bar{\mathbf{K}}_m^{ba} (\bar{\mathbf{K}}_m^{aa})^{-1} \bar{\mathbf{K}}_m^{ab} \mathbf{f}], \quad \mathbf{f} = \mathbf{A} \mathbf{M} \mathbf{e}_1 \quad (41)$$

In order to compute $\bar{\mathbf{K}}_m^{bb} \mathbf{f}$ and $\bar{\mathbf{K}}_m^{ab} \mathbf{f}$, it suffices to do the following matrix-vector multiplication

$$\begin{bmatrix} \bar{\mathbf{K}}_m^{aa} & \bar{\mathbf{K}}_m^{ab} \\ \bar{\mathbf{K}}_m^{ba} & \bar{\mathbf{K}}_m^{bb} \end{bmatrix} \begin{bmatrix} \mathbf{0} \\ \mathbf{f} \end{bmatrix} = \begin{bmatrix} \bar{\mathbf{K}}_m^{ab} \mathbf{f} \\ \bar{\mathbf{K}}_m^{bb} \mathbf{f} \end{bmatrix} \equiv \begin{bmatrix} \mathbf{g} \\ \mathbf{h} \end{bmatrix} \quad (42)$$

The first column of \mathbf{T}_M is then given by

$$\mathbf{T}_M^1 = \frac{1}{h} \mathbf{M}^T \mathbf{A}^T [\mathbf{h} - \bar{\mathbf{K}}_m^{ba} (\bar{\mathbf{K}}_m^{aa})^{-1} \mathbf{g}] \quad (43)$$

To compute $(\bar{\mathbf{K}}_m^{aa})^{-1} \mathbf{g}$, it suffices to solve the following linear system

$$\begin{bmatrix} \bar{\mathbf{K}}_m^{aa} & \bar{\mathbf{K}}_m^{ab} \\ \bar{\mathbf{K}}_m^{ba} & \bar{\mathbf{K}}_m^{bb} \end{bmatrix} \begin{bmatrix} \mathbf{u} \\ \mathbf{0} \end{bmatrix} = \begin{bmatrix} \mathbf{g} \\ \mathbf{0} \end{bmatrix} \quad (44)$$

Finally, to compute $\bar{\mathbf{K}}_m^{ba} (\bar{\mathbf{K}}_m^{aa})^{-1} \mathbf{g} = \bar{\mathbf{K}}_m^{ba} \mathbf{u}$, the following matrix-vector multiplication is used

$$\begin{bmatrix} \bar{\mathbf{K}}_m^{aa} & \bar{\mathbf{K}}_m^{ab} \\ \bar{\mathbf{K}}_m^{ba} & \bar{\mathbf{K}}_m^{bb} \end{bmatrix} \begin{bmatrix} \mathbf{u} \\ \mathbf{0} \end{bmatrix} = \begin{bmatrix} \bar{\mathbf{K}}_m^{aa} \mathbf{u} \\ \bar{\mathbf{K}}_m^{ba} \mathbf{u} \end{bmatrix} \equiv \begin{bmatrix} \mathbf{m} \\ \mathbf{l} \end{bmatrix} \quad (45)$$

To summarize, the first column of the consistent tangent moduli is given by

$$\mathbf{T}_M^1 = \frac{1}{h} \mathbf{M}^T \mathbf{A}^T (\mathbf{h} - \mathbf{l}) \quad (46)$$

which consists of the solution of a linear system Eq.(44) and two matrix-vector multiplications.

In the same manner, the second column of \mathbf{T}_M is computed with $\mathbf{e}_2 = [0 \ 1]^T$. As demonstrated, the procedure we follow does not directly need matrix inversion. Furthermore, all the calculation involves only the total RVE matrix. No explicit sub-matrix is needed. For ease of implementation, the procedure is given in Box 2.

Remark 4.2. *It is emphasized that in [57] authors have proposed a perturbation method to compute the macroscopic tangent in a multilevel finite element setting as an alternative to the standard condensation procedure. Their reasoning was to avoid the large computer memory required to store the microscopic sub-matrices. We have presented an implementation in which the standard condensation is utilized that does not need to allocate any new sub-matrix.*

4.3. Handling arbitrary macro-crack direction

The discussion so far applies to the case in which the angle (\mathbf{n}, x_m^1) is zero. If this is not the case as shown in Fig.(9a), there are two options. As the first option, the geometry of the micro-model is rotated in order to align it with the macro-crack, see Fig.(9b). According to the second option (adopted in this work), that is applicable to materials with a microstructure having an isotropic geometry (e.g., random microstructure as the target material in this work), the position of the micro-model is fixed, Fig.(9c), and we proceed as follows. The global macro-jump vector is transformed to the local coordinate system associated to a point on the crack surface by

$$[\mathbf{u}]_{ns} = \mathbf{Q}[\mathbf{u}]_M \quad (47)$$

This local jump vector is then used as boundary condition imposed on the RVE's boundaries. The first component of $[\mathbf{u}]_{ns}$ is used as boundary condition along the x_m^1 direction and the

Box 2 Computation of the macroscale cohesive tangent with the probing method

1. Assembling the micro stiffness \mathbf{K}_m
2. Constructing the modified matrix $\bar{\mathbf{K}}_m$ using Eq.(35) ⁽¹⁾
3. Initialize $3n \times 1$ vectors $\mathbf{d} = \mathbf{0}$ and $\mathbf{f}_1 = \mathbf{0}$, n is the total number of micro nodes
4. For $i = 1, 2$, do
 - (a) Compute $\mathbf{f} = \mathbf{M}\mathbf{e}_i$
 - (b) Set $\mathbf{d}[b] = \mathbf{f}$
 - (c) Compute $\mathbf{rhs} = \bar{\mathbf{K}}_m\mathbf{d}$, then $\mathbf{g} = \mathbf{rhs}[a]$, $\mathbf{h} = \mathbf{rhs}[b]$
 - (d) Solve the linear system $\bar{\mathbf{K}}_m\mathbf{u} = \mathbf{f}_1$ with $\mathbf{f}_1[a] = \mathbf{g}$ ⁽²⁾
 - (e) Compute $\mathbf{rhs} = \bar{\mathbf{K}}_m\mathbf{u}$, then $\mathbf{m} = \mathbf{rhs}[a]$, $\mathbf{l} = \mathbf{rhs}[b]$
 - (f) Compute column i as $\mathbf{T}_M^i = \frac{1}{h}\mathbf{M}^T(\mathbf{h} - \mathbf{l})$
5. End for

⁽¹⁾ This is not needed when using an iterative solver.

⁽²⁾ With homogeneous boundary conditions $\mathbf{u}[b] = \mathbf{0}$.

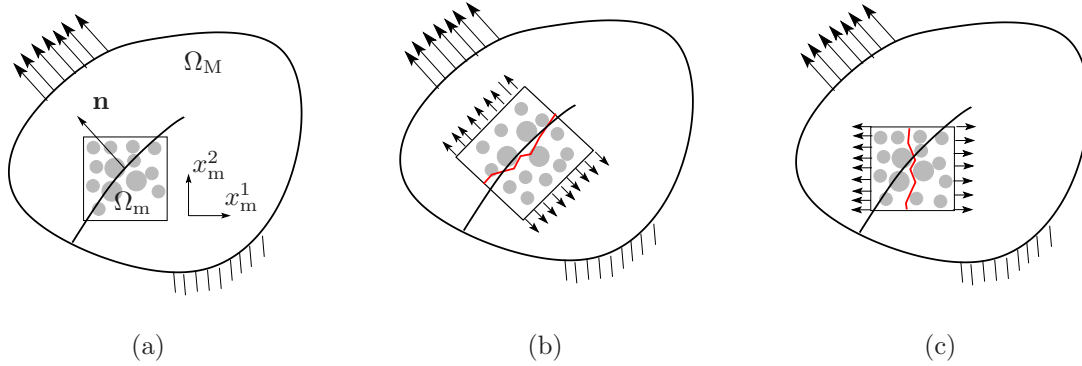


Figure 9. Arbitrary macro crack orientation (a), rotated RVE geometry (b) and (c)-fixed RVE geometry (applicable to microstructure having isotropic geometry).

second one along the x_m^2 direction. After solving the RVE problem, one obtains the macro-traction and tangent in the local coordinate system, \mathbf{t}_{ns} and \mathbf{T}_{ns} , using Eq.(20a) and Eq.(20b), respectively, and they are transformed back into the global coordinate system as follows

$$\mathbf{t}_M = \mathbf{Q}\mathbf{t}_{ns}, \quad \mathbf{T}_M = \mathbf{Q}\mathbf{T}_{ns}\mathbf{Q} \quad (48)$$

with \mathbf{Q} being the orthogonal transformation matrix, see [58].

It should be emphasized that the option using rotated micro-model geometry, see Fig. (9b), must be used for materials having a microstructure with a preferential direction (e.g., masonry).

Remark 4.3. *Note that option described in Fig. (9b) is general i.e., can be applied to any materials whereas option given in Fig. (9c) saves computational efforts for materials with isotropic geometry. It is emphasized that the proposed approach, see Fig. (9c), would not work for non-proportional loadings. For example, an initial loading causes damage in the micro-*

sample, then unloading occurs, and the load direction is changed, subsequently causing the micro-sample to be further damaged. Because of the first damaging phase the micro-sample becomes anisotropic thus violating the assumption on the isotropy of the micro-sample upon which the proposed approach has been developed i.e., the proposed algorithm would be invalid.

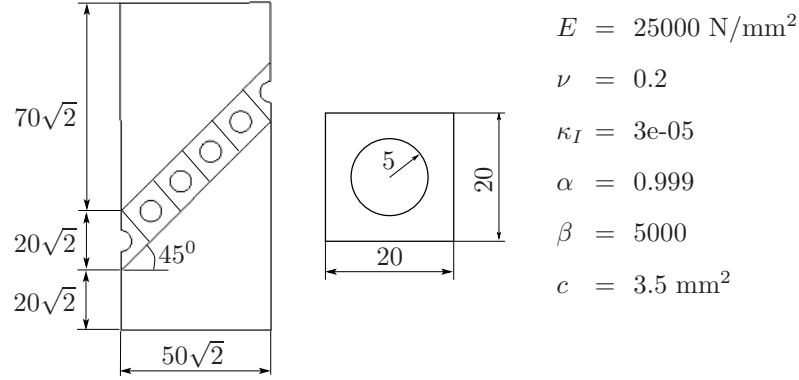


Figure 10. Inclined material layer having a periodic voided microstructure. Unit of length is mm.

As an example to illustrate the idea, let us consider the problem shown in Fig.(10) which consists of two homogeneous elastic adherents joined together by a voided damageable adhesive layer. The sample is fixed in vertical direction at the bottom edge and in the horizontal direction on the left and right edges. These BCs ensure that a homogeneous state of deformation is obtained for all integration points on the adhesive crack. The simulation is performed under a plane stress condition by means of a uniform vertical displacement being imposed on the top edge. Finite element meshes of the Direct Numerical Simulation (DNS) model and the multiscale model (case I model since $w = t_{\text{adh}} = 20$ mm) are given in Fig.(11). In this paper, the four-node linear interface element with Newton-Cotes integration (2 integration points) rule is adopted to model the adhesive crack. Figure (12) gives the comparison of the load-displacement curves of the DNS and multiscale models. The multiscale solution properly follows the DNS solution. We attribute the small discrepancy between those two solutions to the mismatch of geometries at the boundaries of the adhesive layer used in DNS and multiscale simulations, see Fig. (13). Damage patterns in the DNS and in the RVEs are shown in Fig. (14).

4.4. Loading/unloading treatment

4.4.1. Adhesive crack-case I Let us first consider Case I (micro sample width w equals t_{adh}). Since $\mathbf{u}_R = \llbracket \mathbf{u} \rrbracket_M$, unloading is handled naturally i.e., macroscale unloading follows microscale unloading. Therefore, no further work is needed.

4.4.2. Adhesive crack-case II/cohesive crack For Case II, we have $\mathbf{u}_R \neq \llbracket \mathbf{u} \rrbracket_M$ and for cohesive cracks, the failure zone averaging scheme fails when unloading occurs (because the active damaged domain Ω_d is empty). For these reasons, loading/unloading is treated with a history variable being the maximum opening displacement ever reached $\llbracket u \rrbracket_M^{\text{max}}$. Assuming secant

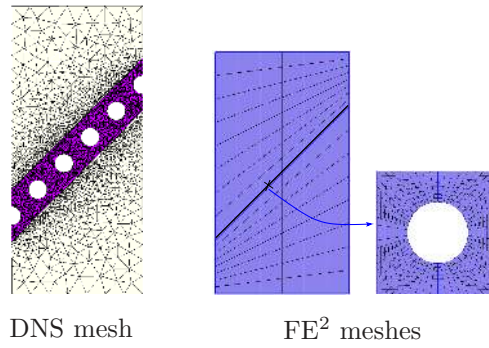


Figure 11. Inclined material layer: DNS mesh and multiscale meshes. The thick line denotes the interface elements.

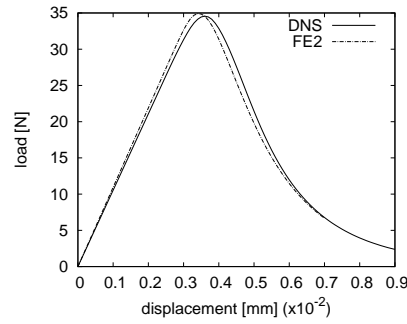


Figure 12. Inclined material layer: comparison of load-displacement curves between DNS and multiscale (case I).

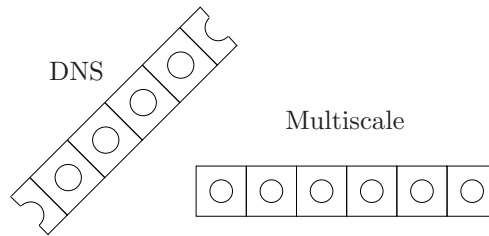


Figure 13. Inclined material layer: Geometry mismatch in DNS and multiscale (case I) models.

unloading, the macro traction is then defined as

$$t_M = \frac{t_M^{\max}}{\llbracket u \rrbracket_M^{\max}} \llbracket u \rrbracket_M \quad (49)$$

since t_M^{\max} cannot be computed from $\llbracket u \rrbracket_M^{\max}$ analytically due to the lack of a phenomenological cohesive law, it is computed from the micro-model corresponding to the state right before unloading occurs. Note that during macro unloading, the micro-model is not loaded and thus

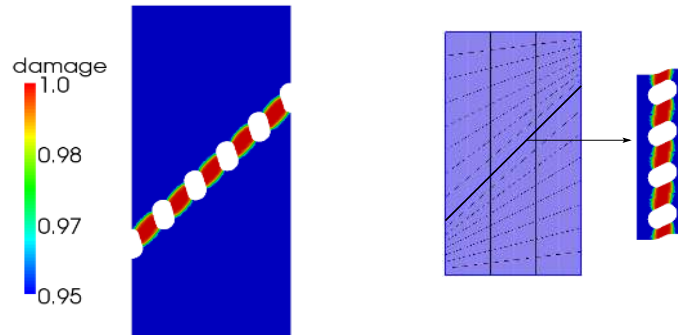


Figure 14. Damage pattern in the DNS (left) and in RVEs associated to interface elements (right).

no micro-BVP is needed to be solved.

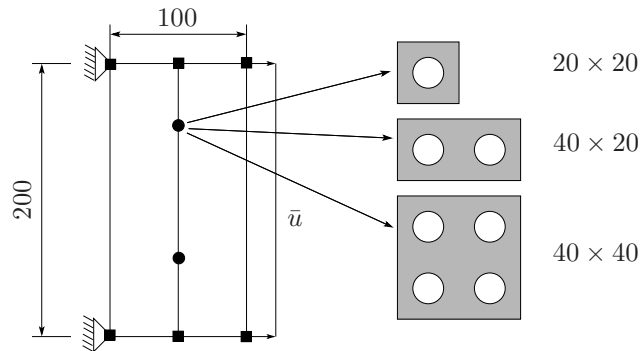


Figure 15. A simple problem (all units in mm) with a vertical material layer having thickness of 40 mm. The layer is made of a periodic voided microstructure. Three RVEs (voids with a radius of 5) shown in the right are investigated.

As an example for handling loading/unloading in a multiscale simulation, we consider a simple test given in Fig.(15) which consists of two adherents joined by an adhesive layer of 40 mm thickness. When the prescribed displacement \bar{u} equals 0.4 mm, the sample is unloaded and then reloaded until final failure of the sample. A plane stress condition is assumed. Material properties of the micro-model can be found in Fig.(10) except the softening slope $\beta = 3000$.

The load-displacement curves shown in Fig.(16) verify, for both case I (micro-models 40×40 and 40×20) and case II (micro-model 20×20) schemes, the objectivity of the macroscale response with respect to the adopted micro-model for loading/unloading excitations.

4.5. Macroscale snapback with dissipation-based arc-length control

Tracing equilibrium paths with snap through and snapback points has been traditionally undertaken by means of path-following methods (also known as arc-length methods), see for instance [59, 60]. A very elegant method, the dissipation-based arc-length method, has been recently introduced in [56, 61] to trace complex equilibrium paths, see [43] for application

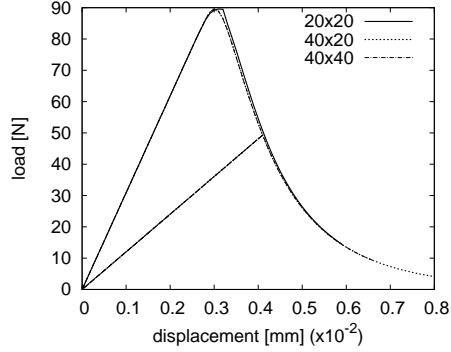


Figure 16. Multiscale cohesive law with unloading behavior.

examples. In this section, we present a preliminary study on resolving macroscopic snapback in a multiscale setting. Note that for the particular material model we are using at the microscale, no microscale snapback has occurred. If this is about to happen, a solution has been reported in [62]. To the best of our knowledge, no multiscale simulation which involves both macroscopic and microscopic snapback has been reported in literature.

According to the dissipation-based arc-length method [56, 61], the macroscale system of equations is given by

$$\begin{aligned} \mathbf{f}_M^{\text{int}}(\mathbf{u}_M) &= \lambda \bar{\mathbf{f}} \\ \phi(\lambda, \mathbf{u}_M) &= 0 \end{aligned} \quad (50)$$

where $\bar{\mathbf{f}}$ is a unit force vector, λ is the so-called load factor and ϕ is a constraint equation that, for a given load step, defines λ in such a manner that a predefined amount of energy $\Delta\tau$ is released. Details can be found in [56, 61]. **Contrary to** other arc-length methods, ϕ is defined in terms of global quantities and hence there is no need to keep tracks of areas where localized nonlinearity is taking place. Usually, $\Delta\tau$ is set to fall within the following bound

$$\Delta\tau_{\min} \leq \Delta\tau \leq \Delta\tau_{\max} \quad (51)$$

for example, the expression $\Delta\tau_{\max} = \delta l_e G_{Ic}$ is often used [61] in a PUM method where a crack is only extended over a single element after a converged step. In a FE^2 setting, $\Delta\tau$ must be chosen smaller because all micro-models must converge. Since a universal rule for $\Delta\tau$ that ensures convergence of the macro-model and all micro-models is missing when the macro-model does not converge, the corresponding macroscale load step is resolved with a smaller $\Delta\tau$.

Figure (17) describes the considered problem that shows macroscopic snapback behavior. The macro-mesh is simply composed of two four-node quadrilateral (Q4) elements with one interface element in between of which behavior is coming from two micro-samples, the $40 \times 20 \text{ mm}^2$ one for the case I scheme and the $20 \times 20 \text{ mm}^2$ one for the case II scheme. A plane stress condition is assumed. The macroscale load-displacement curves obtained with two different values of $\Delta\tau_{\min}$ are given in Fig. (18).

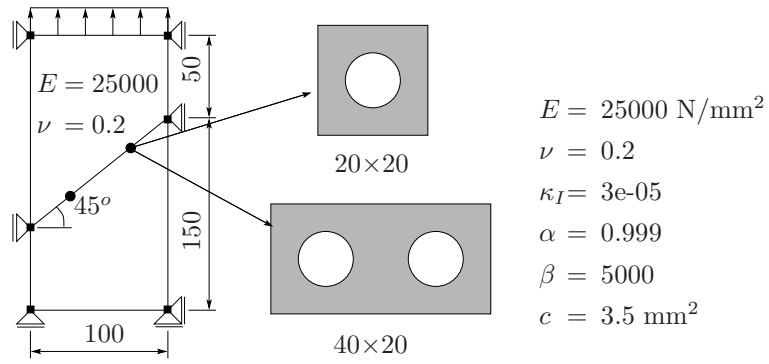


Figure 17. A simple test with macro-snapback. The voids have a radius of 5. Unit of length is mm.

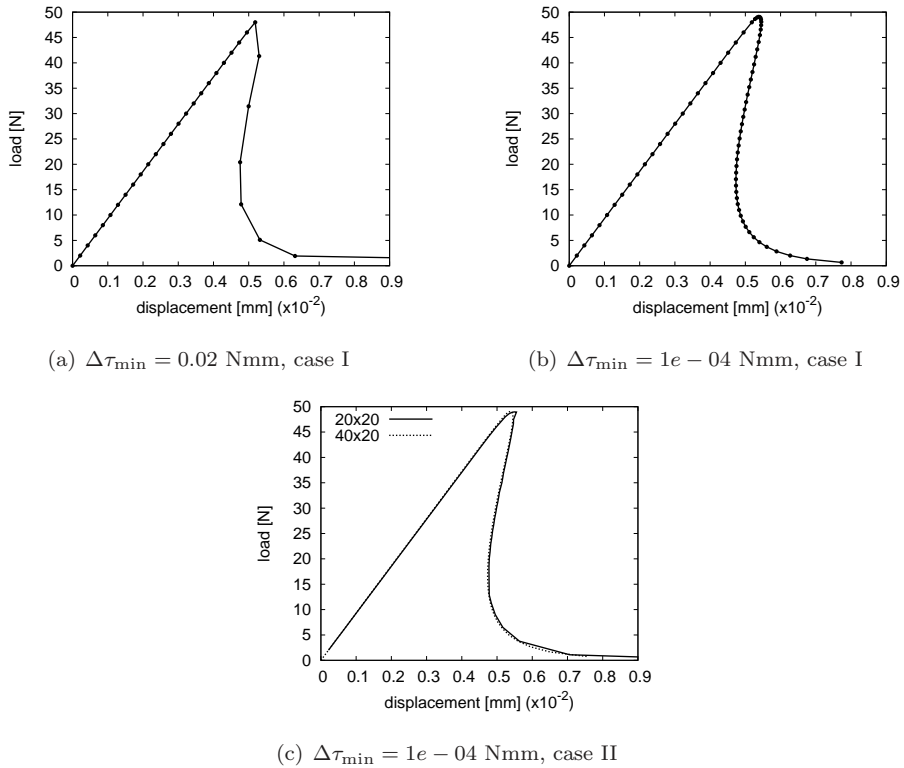


Figure 18. Handling macroscopic snapback with a dissipation-based arc-length control in the multiscale adhesive crack scheme.

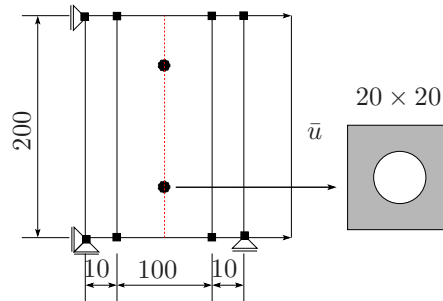


Figure 19. A simple problem with one cohesive crack that shows macroscopic snapback. All units are in mm.

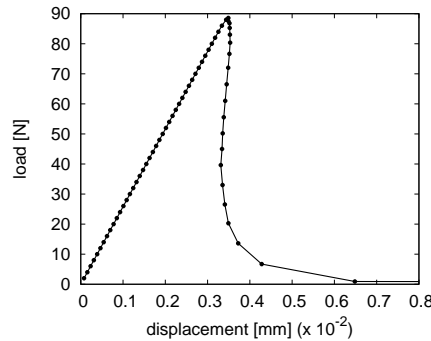


Figure 20. Handling macroscopic snapback with a dissipation-based arc-length control in the multiscale cohesive crack scheme.

For cohesive cracks, let us consider the problem depicted in Fig.(19). Material parameters for the micro-model are given in Fig.(17) except $\beta = 6000$. A plane stress condition is assumed. The load-displacement curve is given in Fig.(20). A value $\Delta\tau_{\min} = 1e - 03$ Nmm was used.

We have shown that the dissipation-based arc-length control presented in [56] can be seamlessly adopted in the proposed multiscale crack modelling framework. **It should be mentioned that secant unloading is the critical assumption for allowing the arc-length control to work.**

5. NUMERICAL EXAMPLES

In this section, four numerical examples are given to demonstrate the performance of the proposed multiscale method. In the first example, a simple macro-sample in uni-axial tension is analyzed. The microstructure is, however, a complex random multi-phase material. The aim of this example is to verify the objectivity of the method with respect to the micro-model size. The convergence property of the presented method is investigated in the second example. The wedge splitting test is analyzed in the third example in which a comparison against a DNS is given. Finally, failure of a single edge notched beam (SEN) which involves the propagation of a

curved crack is given in the final example. Finite element meshes used in this section have been generated using Gmsh [63] except the concrete micro-samples in the first and fourth example that have been created using SPACE [64].

5.1. RVE's existence test

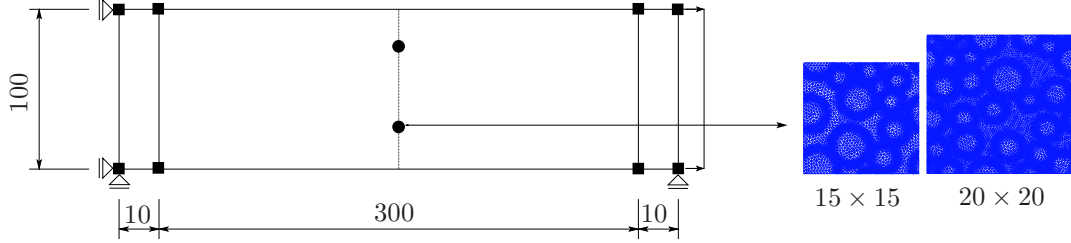


Figure 21. Geometry, finite element discretization of the macro-model (left) and micro-samples (right) for the RVE's existence test. All units are in mm.

		Matrix	Aggregate	ITZ
E	$[\text{N}/\text{mm}^2]$	25000	30000	20000
ν	$[-]$	0.2	0.2	0.2
κ_I	$[-]$	5e-06	0.5	3e-06
α	$[-]$	0.999	0.999	0.999
β	$[-]$	1500	1500	1500
c	mm^2	0.2	0.2	0.2

Table I. Material parameters of different phases of the random heterogeneous material.

In order to verify the objectivity of the multiscale solution with respect to the micro-model size, the problem as shown in Fig.(21) is devised. Upon satisfaction of the failure criterion, $\sigma_M^I \geq 0.97\sigma_m^{\text{ult}}$, a vertical crack is initiated in the middle element (we allowed only one crack in this example). The behavior of this crack is coming from FE computations realized on two micro-samples made of a three-phase material** (aggregate, matrix and interfacial transition zone (ITZ)) of which material parameters can be found in Table (I). These samples correspond to a 45% volume fraction of aggregates (of which radius varies from 2.5 mm to 5.0 mm). The width of the ITZ is 0.25 mm. The microscale FE meshes consist of 10 052 and 18 208 three-node triangle elements (T3 elements) for the $15 \times 15 \text{ mm}^2$ and the $20 \times 20 \text{ mm}^2$ sample, respectively. A plane strain condition is assumed for the micro-models. The effective elastic moduli \mathbf{D}_0 computed using the computational homogenization approach described in Section 3.1.2 are

**This is the microstructure of concrete at mesoscale.

$$\mathbf{D}_0^{15} = \begin{bmatrix} 29903.0 & 7485.55 & -1.15865 \\ 7485.55 & 29905.9 & 0.919313 \\ -1.15865 & 0.919313 & 11213.6 \end{bmatrix}, \mathbf{D}_0^{20} = \begin{bmatrix} 29804.3 & 7456.68 & 0.135379 \\ 7456.68 & 29812.1 & 0.0845691 \\ 0.135379 & 0.0845691 & 11173.7 \end{bmatrix} \quad (52)$$

for micro-sample $15 \times 15 \text{ mm}^2$ and $20 \times 20 \text{ mm}^2$, respectively.

The objectivity of the macroscale solution with respect to the micro-model size can be judged from Fig.(22) which shows the macroscale load-displacement curves obtained with two micro-samples. It is emphasized that micro-samples smaller than $15 \times 15 \text{ mm}^2$ would yield a different macroscale solution since these micro-samples are not large enough [33]. The homogenized cohesive laws are also given in this figure. Note that since the crack was inserted slightly before the ultimate load of the micro-model, the homogenized cohesive laws are not initially rigid as conventional cohesive laws.

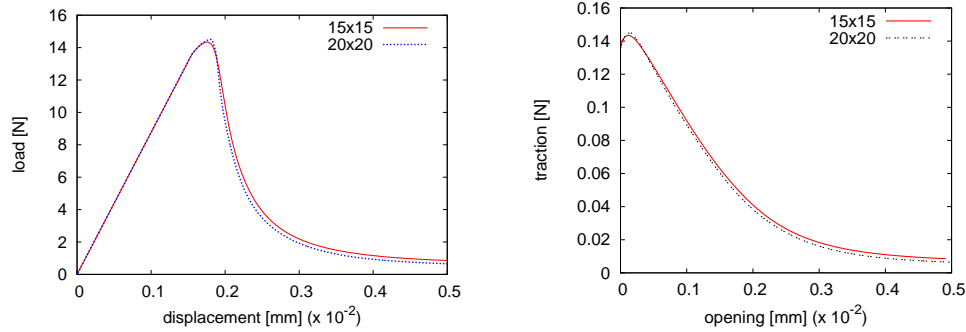


Figure 22. RVE's existence test: objective macroscopic load-displacement diagrams obtained with various microstructures (left) and homogenized traction-opening laws (right).

Remark 5.1. *The number of load increments required to solve the macroscopic BVP from the moment of crack nucleation until final failure is denoted as n . Each macroscale load increment is done with an averaged number of m Newton-Raphson iterations. For one macroscale Newton-Raphson iteration one has to solve $2p$ micro-BVPs (in this example there is only one crack segment with 2 integration points). Therefore, the total number of micro-BVPs is $n \times m \times 2p$. Considering that $n = 60$, $m = 4$ and $p = 2$, then for this simple example one has to solve 480 micro-BVPs of dimension 30 156 dofs (for the $15 \times 15 \text{ mm}^2$ sample). Needless to say, any advanced techniques that is capable of reducing the computational cost of the proposed multiscale scheme is necessary. One promising avenue is model order reduction methods applied to the microscale damage model. Basic ideas have been set in [7, 65].*

5.2. Convergence properties of the multiscale scheme

This example aims at giving some hints for the convergence properties of three multiscale schemes presented before: adhesive crack scheme (case I and case II) and cohesive crack scheme. The use of a consistent tangent matrix at the microscale yields an optimal quadratic convergence rate for the microscale problem and hence convergence properties of the microscale

problem are standard and not reported. Rather, we focus on the convergence performance of the Newton-Raphson iterative method at the macroscale and on the one of the iterative scheme used to solve Eqs.(19) and (27).

For adhesive cracks, let us reconsider the problem given in Fig.(15), section 4.4. Material properties of the micro-model can be found in Fig.(10). The sample is loaded under displacement control with a constant step $\Delta u = 0.0001$ mm. For the case I scheme (micro-model is 40×20 mm²), the load-displacement diagram and the number of Newton-Raphson (NR) iterations required for each macroscale load increment is given in Fig.(23). A quadratic convergence rate can be observed from Table (II). Note that load step 31 is a difficult one since the slope is almost vertical. That explains why 6 NR iterations were required for this step.

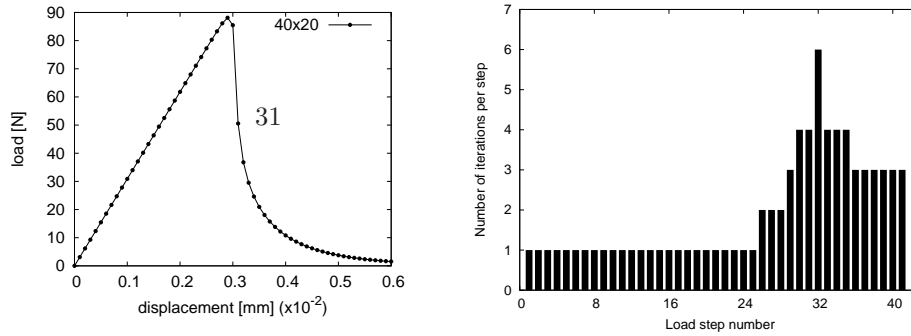


Figure 23. Adhesive scheme-case I: Load-displacement curve and the Newton-Raphson iterations per macroscale load step.

The residual \mathbf{r} is the standard scaled residual between the current iteration i and the first iteration, which reads

$$\mathbf{r} = \frac{\|\mathbf{f}_M^{\text{ext}} - \mathbf{f}_M^{\text{int}}\|_i}{\|\mathbf{f}_M^{\text{ext}} - \mathbf{f}_M^{\text{int}}\|_1} \quad (53)$$

where $\|\cdot\|$ is the L_2 norm.

Step no.	Iteration no.	Residual \mathbf{r}
31	1	4.6334e-02
	2	2.4752e-02
	3	2.5577e-02
	4	3.5018e-03
	5	1.1404e-04
	6	1.3562e-07
36	1	3.3328e-02
	2	1.7055e-04
	3	4.3285e-09

Table II. Adhesive scheme-case I: performance of the macroscale Newton-Raphson method.

We now turn our attention to the adhesive crack-case II scheme. In this case, the 20×20 mm² micro-model is used. Figure (24) shows the load-displacement diagram and the number of NR iterations required for each macroscale load increment. We attribute the need of a large number of NR iterations (19) for macroscale load step 31 to two facts. The first one is the almost vertical slope of the load-displacement curve at that point. The second is that step 31 is the transition step from a hardening regime to a softening regime. Let us recall that we use two different schemes for the hardening and the softening parts, Section 3.2.2. By using a less steep softening slope $\beta = 3000$ (so far $\beta = 5000$ was used), Figure (25) obviously shows that the maximum number of NR iterations is just 4.

The bottom part of Fig.(24) gives the number of micro-BVPs that are solved for every macroscale NR iterations. As can be seen, far from the peak, the micro-BVP is solved only one time per macroscale NR iteration which is similar to standard FE² methods.

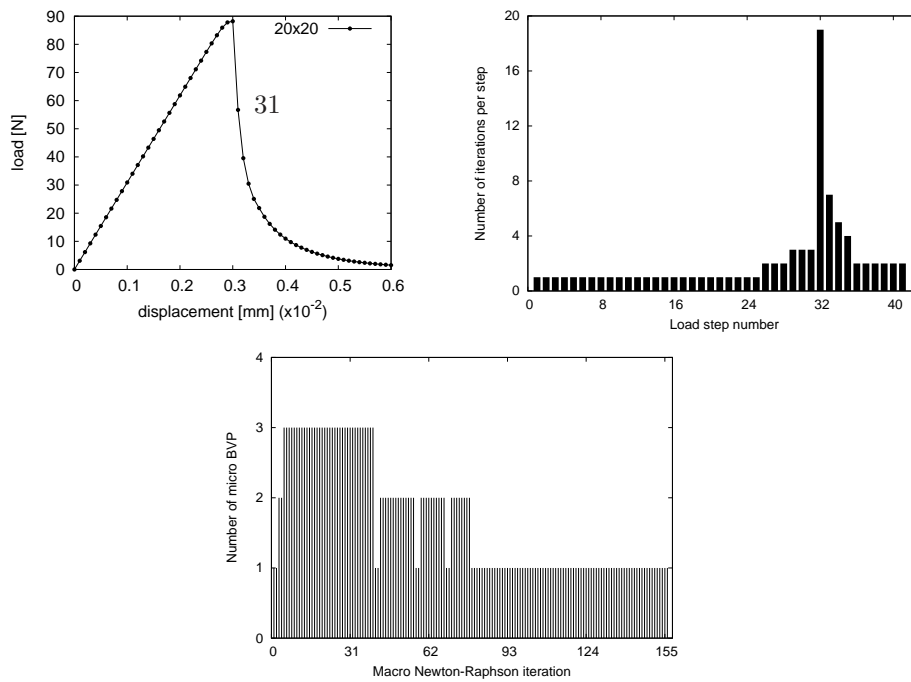


Figure 24. Adhesive scheme-case II: load-displacement curve (top left), Newton-Raphson iterations per macroscale step (top right) and number of micro-BVPs for every macroscale Newton-Raphson iterations (bottom).

For the cohesive crack homogenization scheme, the problem given in Fig.(19) is considered again. Material properties of the micro-model can be found in Fig.(10) except $\beta = 1000$ to have a smooth macroscale equilibrium path. Figure (26) shows the load-displacement diagram and the number of NR iterations required for each macroscale load increment. Three NR iterations are needed for macroscale steps round the peak. The reduction in residuals for two macroscale load increments around the peak is tabulated in Table (III). The bottom part of Fig.(26) gives the number of micro-BVPs that are solved for every macroscale NR iterations. Far from the

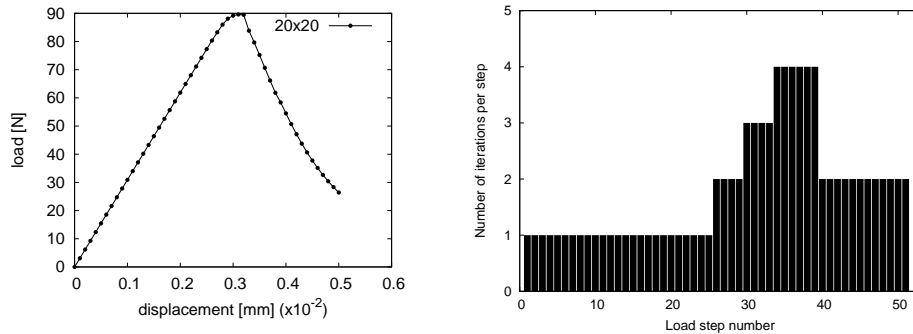


Figure 25. Adhesive scheme-case II, smooth response with $\beta = 3000$: load-displacement curve, Newton-Raphson iterations per macroscale step.

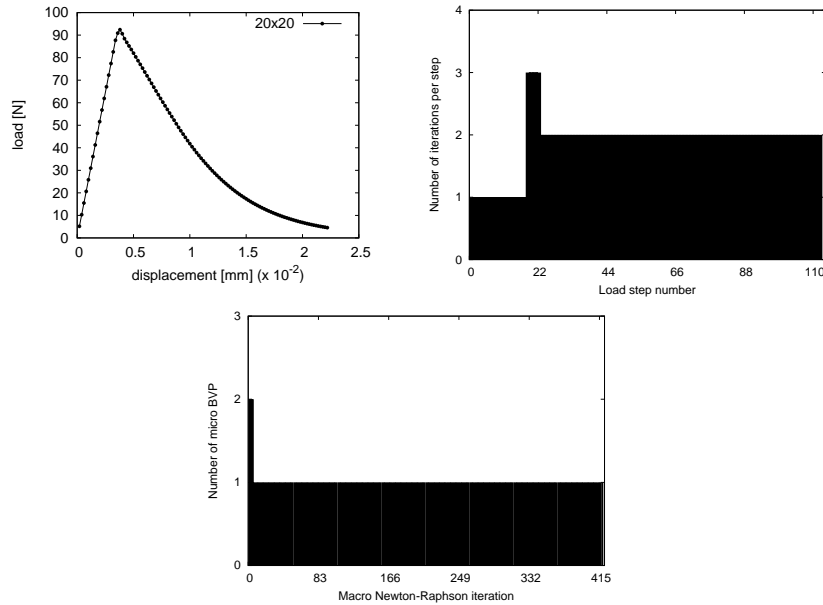


Figure 26. Cohesive crack scheme: load-displacement curve (top left), Newton-Raphson iterations per macroscale step (top right) and number of micro-BVPs for every macroscale Newton-Raphson iterations (bottom).

peak, the micro-BVP is solved only one time per macroscale NR iteration which is similar to standard FE^2 methods.

5.3. Wedge splitting test

The wedge splitting test, given in Fig.(27), is studied in this example. The sample is made of a matrix-fiber material (with a weak transition zone, ITZ, to model matrix-fiber interface debonding). In order to reduce the computational cost, the microstructure is only explicitly

Step no.	Iteration no.	Residual r
17	1	1.0189e-02
	2	6.9791e-04
	3	2.5718e-06
18	1	5.8094e-03
	2	1.2804e-04
	3	3.3568e-08

Table III. Cohesive crack scheme: performance of the macroscale Newton-Raphson method.

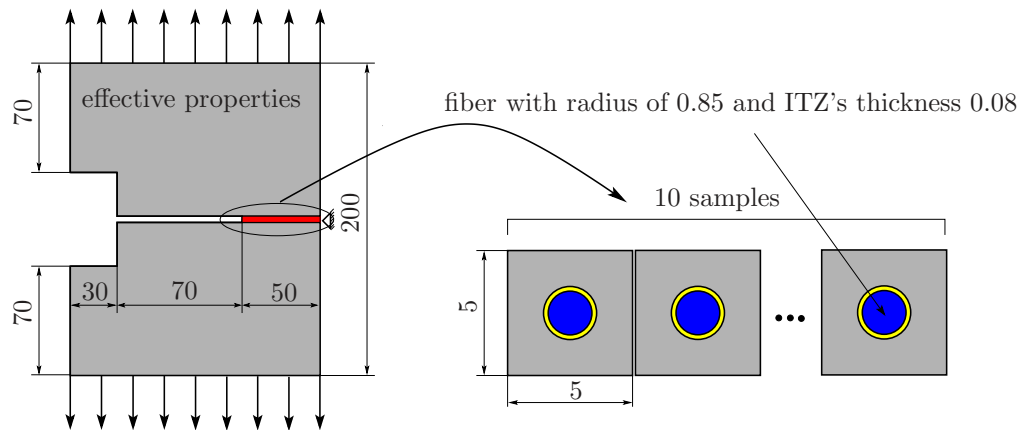


Figure 27. Wedge splitting test: geometry (units in mm) and boundary conditions.

resolved in the region in front of the notch where the crack is expected to develop and grow. The rest (shaded region) is modelled as homogeneously linear elastic with effective properties (the Young's modulus is 12647.66 N/mm^2 and the Poisson's ratio is 0.2). Material in the red region follows the isotropic non-local damage model described in Section 2.2.1 with material parameters being given in Tab.(IV). The analysis is performed under a plane stress state with displacement control. This example is specially designed in order to make a comparison of the proposed multiscale model with a DNS. A simple microstructure is taken and a single localization band is promoted.

The FE discretization of the DNS model, shown in Fig.(28), consists of 25 368 three-node triangle elements and 12 778 nodes (36 366 dofs). Finite element meshes of the macro-model and micro-model in a multiscale simulation are given in Fig.(29). When $\sigma_M^I \geq 0.999\sigma_m^{\text{ult}}$, the macro-crack initiates/propagates. In this example, due to symmetry, the crack direction at the macroscale is forced to be horizontal.

Evolution of damage in the DNS and evolution of the macro-crack in the FE^2 model is shown in Figs.(30-31). An observation was made from Fig.(30) that the macro-crack in the multiscale model runs slightly behind the localization band in the DNS. We attribute this to two facts namely (i) the macroscopic load increments are larger for the FE^2 simulation than for the DNS and (ii) the difference in the failure criterion- in DNS, a strain-based damage

		Matrix	Fiber	ITZ
E	[N/mm ²]	25000	30000	20000
ν	[-]	0.2	0.2	0.2
κ_I	[-]	5e-05	0.5	3e-05
α	[-]	0.999	0.999	0.999
β	[-]	100	100	100
c	mm ²	0.005	0.005	0.005

Table IV. Material parameters of different phases of the fiber-reinforced composite.

initiation criterion was used and in FE² a stress-based crack initiation criterion was adopted. It can be observed from Fig.(32) that boundary effects are still not properly handled in the multiscale model. A remedy is to apply periodic BCs only for interior RVEs (e.g., RVEs far from the boundaries) and better tailored BCs for boundary RVEs.

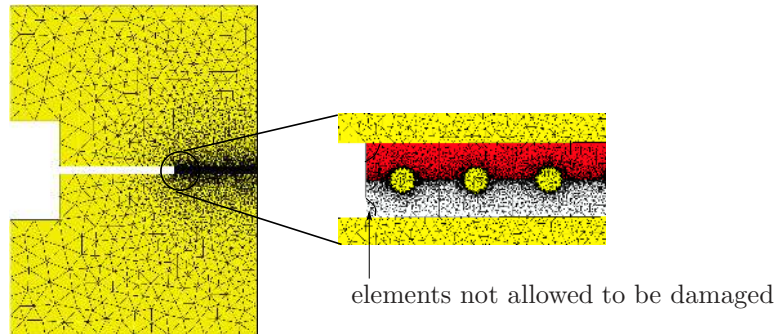


Figure 28. Wedge splitting test: FE mesh of the DNS model (25 368 three-node triangle elements). Elements of the matrix phase in the upper part (red color) are not allowed to be damaged.

Comparison of the load-displacement curves of the DNS and multiscale model (denoted by FE²) is depicted in Fig.(33). The peak load obtained with the DNS is 48.70 N while the peak load obtained with the multiscale model is 48.36 N. The curve associated to the multiscale model is not smooth due to two facts (i) the macroscopic load increment steps are large (to reduce the computation time) and (ii) the mesh of the macro-model is quite coarse (keep in mind that in our PUM implementation, the crack grows element-wise). It is emphasized that in order to make a fair comparison between the DNS and the FE², we have, in the DNS, prevented damage from starting in the corners, see Fig.(28).

Concerning the computational cost, the DNS time was 14 hours while the FE² time was only 4 hours i.e., 3 times faster.

5.4. Single edge notched beam

As an example of a curved propagating crack analysis in the presented multiscale cohesive crack framework, let us consider the single edge notched beam given in Fig.(34). This problem has been studied experimentally in [66] and numerically in a monoscale setting by, for instance,

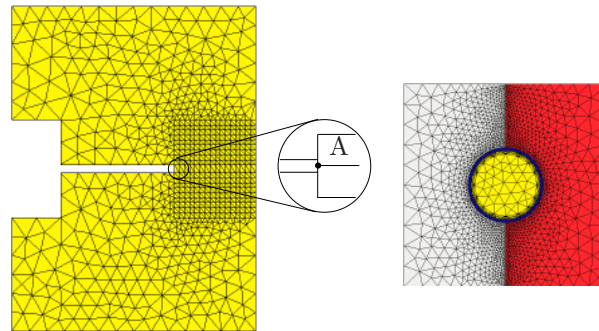


Figure 29. Wedge splitting test: FE meshes of the multiscale model. Macro-mesh consists of 1426 three-node triangle elements whereas micro-mesh composed of 4092 T3 elements. A crack is initiated at point A and grows horizontally to the right edge. In the RVE, elements of the matrix phase in the right part (red color) are not allowed to be damaged. Since the macro-crack direction is horizontal whereas the micro localization band is vertical, the algorithm given in Section 4.3 is used.

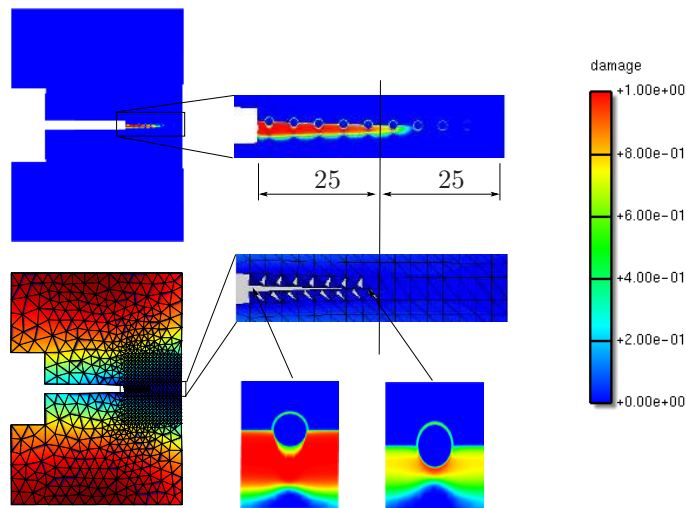


Figure 30. Wedge splitting test: damage pattern in the DNS model (top) and crack path with damaging RVEs in the FE^2 model at the peak.

[40] and in a multiscale setting by [29, 31]. In [31], the authors have studied the influence of the microstructure on the macroscale ultimate load. The post-peak response have not therefore been reported. Here, we focus on the issue of robustness of the proposed multiscale scheme. The aim is to show that a complete multiscale analysis for curved crack propagation can be achieved. No comparison against a DNS is therefore performed.

The beam is made of a concrete material. The behavior of the macro-crack, that is initiated from the lower-right part of the notch and propagates in a curved trajectory toward to the right of the lower-right support, is coming from microscale FE computations performed on a $10 \times 10 \text{ mm}^2$ micro-model shown in Fig.(35b). The FE discretization is given in Fig.(35). The load platens are modelled as steel. A plane stress condition is assumed for the micro-model.

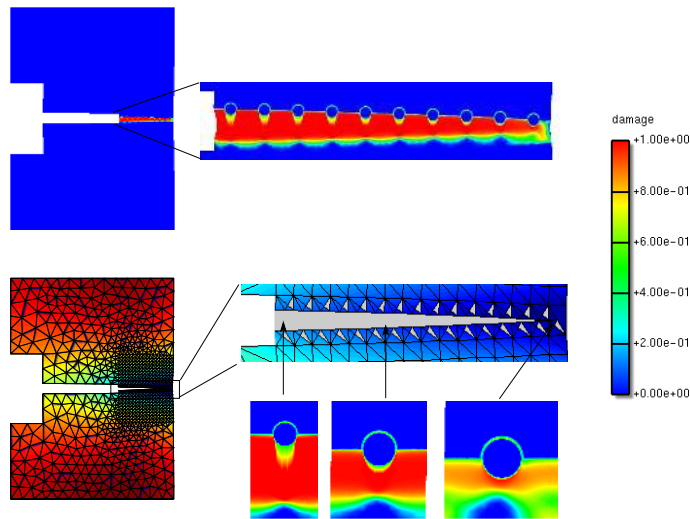


Figure 31. Wedge splitting test: damage pattern in the DNS model (top) at the moment the localization band approaches the right edge of the specimen and crack path with damaging RVEs in the FE² model.

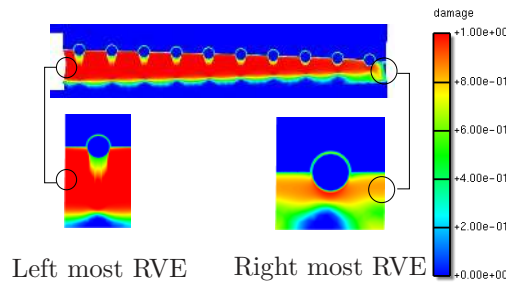


Figure 32. Boundary effects: periodic boundary conditions are not suitable for boundary RVEs.

Material parameters for the constituents of the three-phase microstructure can be found in Table (I) except $c = 0.1 \text{ mm}^2$. When the maximum macroscale principal stress exceeds 99% σ_m^{ult} , the crack initiates or propagates in a direction determined using the non-local stress field at the crack tip, Section 3.1.1. To deal with a curved crack as in this example in which the crack direction is not aligned to the micro-sample the algorithm given in Section 4.3 is used.

The analysis is performed using the dissipation-based arc-length method [56] together with the sub-stepping scheme proposed in [67]. The sub-stepping technique allows the use of relatively large macroscale load increments which dramatically reduces the computational cost of FE² computations. The basic idea of this scheme when applied to the multiscale cohesive crack model is whenever the solution for the micro-BVP, Eq.(19₁), could not be obtained (the corresponding macroscale load increment is big), the displacement being imposed on the RVE is divided into sub-steps. It is emphasized resolving one diverged micro-model with sub-steps is much cheaper than resolving the macro-model with a smaller macro load increment.

The deformed shape of the SEN beam is given in Fig.(36) in which the curved crack path as

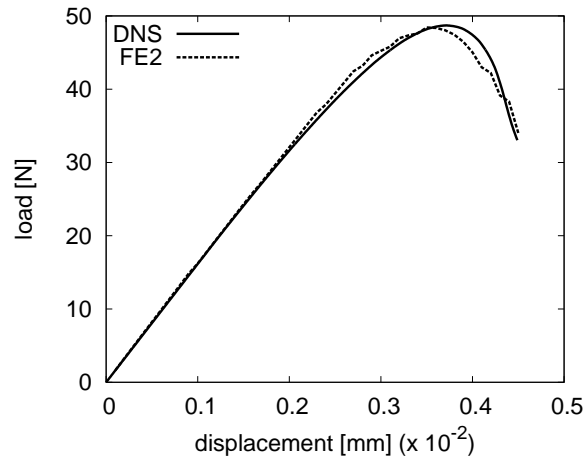


Figure 33. Wedge splitting test: comparison of load-displacement curves between the DNS and the multiscale cohesive crack scheme.

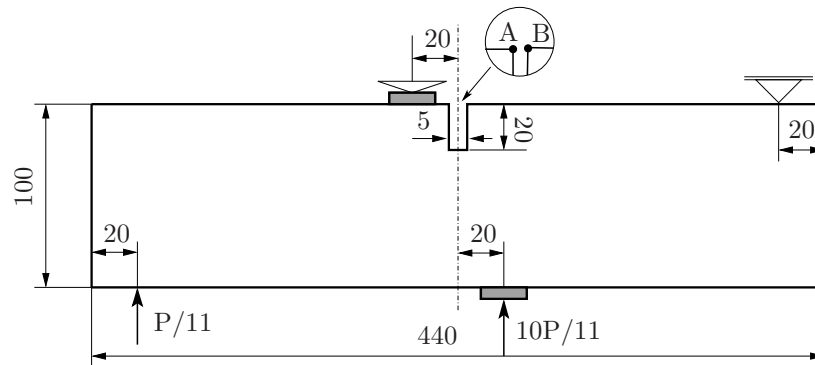


Figure 34. Single edge notched beam (SEN): geometry (all units are in mm), boundary conditions. The depth of the beam is 100 mm. The crack mouth sliding displacement (CMSD) is defined as the difference in vertical displacement of points A and B.

experimentally observed is captured well. The response of the SEN beam, measured in terms of the load P versus the CMSD, is given in Fig.(37).

6. CONCLUSIONS

In this manuscript, details concerning implementational and computational aspects of a multiscale cohesive/adhesive crack modelling framework using computational homogenization have been presented. The behavior of the macroscale cracks is derived from finite element computations realized on microscale samples in which the underlying heterogeneous microstructure that undergoes localized damage is explicitly taken into account. Various

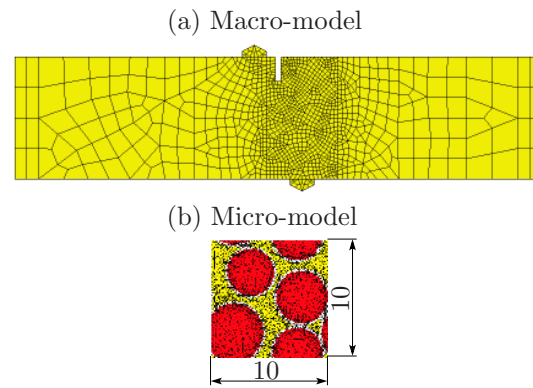


Figure 35. The SEN beam: FE meshes of the macro-model (1219 Q4 elements) and micro-model (5280 T3 elements).

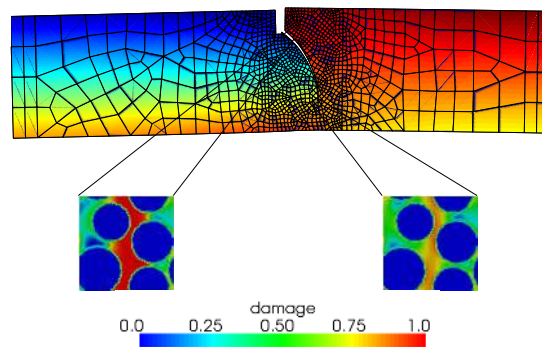


Figure 36. The SEN beam: deformed configuration of the beam (magnified by a factor of 500) and snapshots of damaging micro-models.

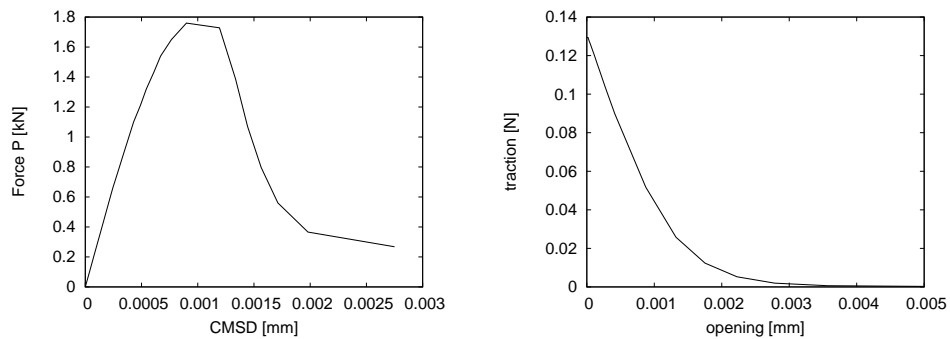


Figure 37. The SEN beam: load P against CMSD (left) and a typical homogenized cohesive law (right).

issues including loading/unloading, macroscopic snapback, arbitrary crack orientation and convergence characteristics of the multiscale scheme were addressed. Efficient implementation of the master-slave method used to solve nonlinear equations with constraints has been discussed. A probing method was given to compute the macroscale tangent matrix from the microscale stiffness matrix without inversion and partition operations. The given numerical examples show that the method can be used for failure analysis of solids with random heterogeneous microstructures undergoing localized damage. It can also be utilized for better designing materials by adjusting the underlying microstructural constituents' shape and properties.

Just like any computational homogenization method, the proposed method is computationally demanding thus limits its applicability. Besides the conventional use of parallel computers, model reduction techniques applied for the microscale damage models would dramatically reduce the computational cost of computational homogenization based multiscale simulations. Model adaptivity, in which microscale computations are made only for integration points in the fracture process zone whilst others points follow an analytical cohesive law, is also capable of enhancing the speed of the proposed method.

ACKNOWLEDGEMENTS

The financial support from the Delft Center for Computational Science and Engineering (DCSE) is gratefully acknowledged. The first author thankfully appreciate the discussion with Dr. Erik Jan Lingem at Habanara, The Netherlands.

REFERENCES

- [1] P. M. Suquet. Local and global aspects in the mathematical theory of plasticity. In A. Sawczuk and G. Bianchi, editors, *Plasticity today: modelling, methods and applications*, pages 279–310, London, 1985. Elsevier.
- [2] R.J.M. Smit, W.A.M. Brekelmans, and H.E.H. Meijer. Prediction of the mechanical behavior of nonlinear heterogeneous systems by multi-level finite element modeling. *Computer Methods in Applied Mechanics and Engineering*, 55:181–192, 1998.
- [3] S. Ghosh, K. Lee, and S. Moorthy. Two scale analysis of heterogeneous elastic-plastic materials with asymptotic homogenization and Voronoi cell finite element model. *Computer Methods in Applied Mechanics and Engineering*, 132:63–116, 1996.
- [4] C. Miehe, J. Schröder, and J. Schotte. Computational homogenization analysis in finite plasticity simulation of texture development in polycrystalline materials. *Computer Methods in Applied Mechanics and Engineering*, 171(3-4):387–418, 1999.
- [5] V. Kouznetsova, W. A. M. Brekelmans, and F. P. T. Baaijens. An approach to micro-macro modeling of heterogeneous materials. *Computational Mechanics*, 27(1):37–48, 2001.
- [6] I. Özdemir, W.A.M. Brekelmans, and M.G.D. Geers. Computational homogenization for heat conduction in heterogeneous solids. *International Journal of Numerical Methods in Engineering*, 73:185–204, 2008.
- [7] E. Monteiro, J. Yvonnet, and Q.C. He. Computational homogenization for nonlinear conduction in heterogeneous materials using model reduction. *Computational Materials Science*, 42(4):704–712, 2008.

- [8] I. Özdemir, W.A.M. Brekelmans, and M.G.D. Geers. FE^2 computational homogenization for the thermo-mechanical analysis of heterogeneous solids. *Computer Methods in Applied Mechanics and Engineering*, 198(3-4):602–613, 2008.
- [9] B.C.N. Mercatoris, Ph. Bouillard, and T.J. Massart. Multi-scale detection of failure in planar masonry thin shells using computational homogenisation. *Engineering Fracture Mechanics*, 76(4):479–499, 2009.
- [10] E. W. C. Coenen, V. G. Kouznetsova, and M. G. D. Geers. Computational homogenization for heterogeneous thin sheets. *International Journal for Numerical Methods in Engineering*, 83(8-9):1180–1205, 2010.
- [11] B.C.N. Mercatoris and T.J. Massart. A coupled two-scale computational scheme for the failure of periodic quasi-brittle thin planar shells and its application to masonry. *International Journal for Numerical Methods in Engineering*, 85(9):1177–1206, 2011.
- [12] C. Oskay. Two-level multiscale enrichment methodology for modeling of heterogeneous plates. *International Journal for Numerical Methods in Engineering*, 80:1143–1170, 2009.
- [13] C. Oskay and G. Pal. A multiscale failure model for analysis of thin heterogeneous plates. *International Journal of Damage Mechanics*, 19:575–610, 2010.
- [14] D. Perić, E.A. de Souza Neto, R.A. Feijóo, M. Partovi, and A.J.C. Molina. On micro-to-macro transitions for multi-scale analysis of non-linear heterogeneous materials: unified variational basis and finite element implementation. *International Journal for Numerical Methods in Engineering*, 2010. In Press.
- [15] F. Feyel. Multiscale FE^2 elastoviscoplastic analysis of composite structures. *Computational Materials Science*, 16(1-4):344–354, 1999.
- [16] F. Feyel. A multilevel finite element method (FE^2) to describe the response of highly non-linear structures using generalized continua. *Computer Methods in Applied Mechanics and Engineering*, 192:3233–3244, 2003.
- [17] K. Matouš, M. G. Kulkarni, and P. H. Geubelle. Multiscale cohesive failure modeling of heterogeneous adhesives. *Journal of the Mechanics and Physics of Solids*, 56(4):1511–1533, 2008.
- [18] C.B. Hirschberger, S. Ricker, P. Steinmann, and N. Sukumar. Computational multiscale modelling of heterogeneous material layers. *Engineering Fracture Mechanics*, 76(6):793–812, 2009.
- [19] M. G. Kulkarni, P. H. Geubelle, and K. Matouš. Multi-scale modeling of heterogeneous adhesives: Effect of particle decohesion. *Mechanics of Materials*, 41(5):573–583, 2009.
- [20] M.V. Cid Alfaro, A.S.J. Suiker, C.V. Verhoosel, and R. de Borst. Numerical homogenization of cracking processes in thin fibre-epoxy layers. *European Journal of Mechanics - A/Solids*, 29(2):119–131, 2010.
- [21] M. G. Kulkarni, K. Matouš, and P. H. Geubelle. Coupled multi-scale cohesive modeling of failure in heterogeneous adhesives. *International Journal for Numerical Methods in Engineering*, 84(8):916–946, 2010.
- [22] M.G.D. Geers, V.G. Kouznetsova, and W.A.M. Brekelmans. Multi-scale computational homogenization: Trends and challenges. *Journal of Computational and Applied Mathematics*, 234(7):2175–2182, 2010.
- [23] I.M. Gitman, H. Askes, and L.J. Sluys. Representative volume: Existence and size determination. *Engineering Fracture Mechanics*, 74(16):2518–2534, 2007.

- [24] I.M. Gitman, H. Askes, and L.J. Sluys. Coupled-volume multi-scale modelling of quasi-brittle material. *European Journal of Mechanics - A/Solids*, 27(3):302–327, 2007.
- [25] T. J. Massart, R. H. J. Peerlings, and M. G. D. Geers. An enhanced multi-scale approach for masonry wall computations with localization of damage. *International Journal for Numerical Methods in Engineering*, 69(5):1022–1059, 2007.
- [26] T.J. Massart, R.H.J. Peerlings, and M.G.D. Geers. Structural damage analysis of masonry walls using computational homogenization. *International Journal of Damage Mechanics*, 16(2):199–226, 2007.
- [27] T.J. Massart and B.C.N. Mercatoris. Assessment of periodic homogenisation-based multiscale computational schemes for quasi-brittle structural failure. *International Journal for Multiscale Computational Engineering*, 7(2):153–170, 2009.
- [28] T. Belytschko, S. Loehnert, and J.H. Song. Multiscale aggregating discontinuities: A method for circumventing loss of material stability. *International Journal for Numerical Methods in Engineering*, 73(6):869–894, 2008.
- [29] T. Belytschko and J.H. Song. Coarse-graining of multiscale crack propagation. *International Journal for Numerical Methods in Engineering*, 81(5):537–563, 2010.
- [30] F.V. Souza and D.H. Allen. Multiscale modeling of impact on heterogeneous viscoelastic solids containing evolving microcracks. *International Journal for Numerical Methods in Engineering*, 82(4):464–504, 2010.
- [31] C.V. Verhoosel, J.J.C. Remmers, M.A. Gutiérrez, and R. de Borst. Computational homogenisation for adhesive and cohesive failure in quasi-brittle solids. *International Journal for Numerical Methods in Engineering*, 83(8-9):1155–1179, 2010.
- [32] V.P. Nguyen, O. Lloberas-Valls, M. Stroeven, and L.J. Sluys. Homogenization-based multiscale crack modelling: from micro-diffusive damage to macro-cracks. *Computer Methods in Applied Mechanics and Engineering*, 200(9-12):1220–1236, 2011.
- [33] V.P. Nguyen, O. Lloberas Valls, M. Stroeven, and L.J. Sluys. On the existence of representative volumes for softening quasi-brittle materials-A failure zone averaging scheme. *Computer Methods in Applied Mechanics and Engineering*, 199(45-48):3028–3038, 2010.
- [34] P.A. Guidault, O. Allix, L. Champaney, and J.P. Navarro. A two-scale approach with homogenization for the computation of cracked structures. *Computers & Structures*, 85(17-18):1360–1371, 2007.
- [35] T. Hettich, A. Hund, and E. Ramm. Modeling of failure in composites by X-FEM and level sets within a multiscale framework. *Computer Methods in Applied Mechanics and Engineering*, 197(5):414–424, 2008.
- [36] S. Eckardt and C. Könke. Adaptive damage simulation of concrete using heterogeneous multiscale models. *Journal of Algorithms & Computational Technology*, 2:275–297, 2008.
- [37] O. Lloberas-Valls, D. J. Rixen, A. Simone, and L. J. Sluys. Multiscale domain decomposition analysis of quasi-brittle heterogeneous materials. *International Journal for Numerical Methods in Engineering*, 2010. (Submitted, October 19, 2010).
- [38] A. Ibrahimbegović and D. Markovič. Strong coupling methods in multi-phase and multi-scale modeling of inelastic behavior of heterogeneous structures. *Computer Methods in Applied Mechanics and Engineering*, 192(28-30):3089–3107, 2003.
- [39] N. Moës, J. Dolbow, and T. Belytschko. A finite element method for crack growth without remeshing. *International Journal for Numerical Methods in Engineering*, 46(1):131–150, 1999.

- [40] G. N. Wells and L. J. Sluys. A new method for modelling cohesive cracks using finite elements. *International Journal for Numerical Methods in Engineering*, 50(12):2667–2682, 2001.
- [41] J. Mergheim, E. Kuhl, and P. Steinmann. A finite element method for cohesive crack modelling. *PAMM*, 4(1):350–351, 2004.
- [42] J.H. Song, P.M.A. Areias, and T. Belytschko. A method for dynamic crack and shear band propagation with phantom nodes. *International Journal for Numerical Methods in Engineering*, 67(6):868–893, 2006.
- [43] F. van der Meer and L. Sluys. A phantom node formulation with mixed mode cohesive law for splitting in laminates. *International Journal of Fracture*, 158(2):107–124, 2009.
- [44] X.P. Xu and A. Needleman. Numerical simulations of fast crack growth in brittle solids. *Journal of the Mechanics and Physics of Solids*, 42(9):1434, 1397, 1994.
- [45] M. Ortiz and A. Pandolfi. Finite-deformation irreversible cohesive elements for three-dimensional crack-propagation analysis. *International Journal for Numerical Methods in Engineering*, 44(9):1267–1282, 1999.
- [46] J. C. J. Schellekens and R. de Borst. On the numerical integration of interface elements. *International Journal for Numerical Methods in Engineering*, 36(1):43–66, 1993.
- [47] G. Beer. An isoparametric joint/interface element for finite element analysis. *International Journal for Numerical Methods in Engineering*, 21(4):585–600, 1985.
- [48] D. V. Kubair and P. H. Geubelle. Comparative analysis of extrinsic and intrinsic cohesive models of dynamic fracture. *International Journal of Solids and Structures*, 40(15):3853–3868, 2003.
- [49] J. Lemaitre. *A course on damage mechanics*. Springer-Verlag, 1996.
- [50] J. Mazars and G.Pijaudier-Cabot. Continuum damage theory - application to concrete. *Journal of Engineering Mechanics Division ASCE*, 115:345–365, 1989.
- [51] R. H. J. Peerlings, R. de Borst, W. A. M. Brekelmans, and J. H. P. de Vree. Gradient enhanced damage for quasi-brittle materials. *International Journal for Numerical Methods in Engineering*, 39:3391–3403, 1996.
- [52] G.Pijaudier-Cabot and Z.P.Bažant. Nonlocal damage theory. *ASME Journal of Applied Mechanics*, 113:1512–1533, 1987.
- [53] J. Simo and J. Ju. Strain- and stress-based continuum damage models-I. formulation. *International Journal of Solids and Structures*, 23(7):821–840, 1987.
- [54] C. Miehe. Computational micro-to-macro transitions for discretized micro-structures of heterogeneous materials at finite strains based on the minimization of averaged incremental energy. *Computer Methods in Applied Mechanics and Engineering*, 192(5-6):559–591, January 2003.
- [55] V. P. Nguyen, M. Stroeve, and L. J. Sluys. A continuous-discontinuous multiscale method for modelling cohesive cracks in random heterogeneous quasi-brittle materials. *Computer Methods in Applied Mechanics and Engineering*, 2011. Submitted.
- [56] M.A. Gutiérrez. Energy release control for numerical simulations of failure in quasi-brittle solids. *Communications in Numerical Methods in Engineering*, 20(1):19–29, 2004.
- [57] I. Temizer and P. Wriggers. On the computation of the macroscopic tangent for multiscale volumetric homogenization problems. *Computer Methods in Applied Mechanics and Engineering*, 198:495–510, 2008.

- [58] K.J. Bathe. *Finite Element Procedures*. Prentice Hall, 1996.
- [59] R. de Borst. Computation of post-bifurcation and post-failure behavior of strain-softening solids. *Computers and Structures*, 25(2):211–224, 1987.
- [60] M. G. D. Geers. Enhanced solution control for physically and geometrically non-linear problems. part II-comparative performance analysis. *International Journal for Numerical Methods in Engineering*, 46(2):205–230, 1999.
- [61] C. V. Verhoosel, J. J. C. Remmers, and M. A. Gutiérrez. A dissipation-based arc-length method for robust simulation of brittle and ductile failure. *International Journal for Numerical Methods in Engineering*, 77(9):1290–1321, 2009.
- [62] T.J. Massart, R.H.J. Peerlings, and M.G.D. Geers. A dissipation-based control method for the multi-scale modelling of quasi-brittle materials. *Comptes Rendus Mécanique*, 333(7):521–527, 2005.
- [63] C. Geuzaine and J.-F. Remacle. Gmsh, a three-dimensional mesh generator with built-in pre- and post-processing facilities. *International Journal for Numerical Methods in Engineering*, 79(11):1309–1331, 2009.
- [64] M. Stroeven and P. Stroeven. SPACE system for simulation of aggregated matter application to cement hydration. *Cement and Concrete Research*, 29(8):1299–1304, 1999.
- [65] P. Kerfriden, P. Gosselet, S. Adhikari, and S. Bordas. Bridging proper orthogonal decomposition methods and augmented Newton-Krylov algorithms: an adaptive model order reduction for highly nonlinear mechanical problems. *Computer Methods in Applied Mechanics and Engineering*, 200(5-8):850–866, 2010.
- [66] E. Schlangen. *Experimental and numerical analysis of fracture processes in concrete*. PhD thesis, Delft University of Technology, 1993.
- [67] D.D. Somer, E.A. de Souza Neto, W.G. Dettmer, and D. Perić. A sub-stepping scheme for multi-scale analysis of solids. *Computer Methods in Applied Mechanics and Engineering*, 198(9-12):1006–1016, 2009.